

# Planar Laser-induced Fluorescence of Nitric Oxide in Isomeric Butanol and Butane Stagnation Flames

Gregory Chung

Master of Engineering

Mechanical Engineering

McGill University

Montreal, Quebec

2012-04-15

A thesis submitted to McGill University in partial fulfillment of the requirements of  
the degree of Master of Engineering

© 2011/2012 Gregory Chung



## ACKNOWLEDGEMENTS

This thesis would not be possible without the huge amounts of support I have received since arriving at McGill. I only hope that my thanks here can adequately express my appreciation for all of the help.

Firstly, I would like to thank my advisor Prof. Jeff Bergthorson for his guidance, wealth of knowledge and constant encouragement. I am grateful to have an advisor who is an inspiring combination of know-how, enthusiasm and patience.

I would like to thank all the members of the Alternative Fuels Lab, past and present, for the technical expertise, ideas and thoughtful (or not) discussions which have undoubtedly contributed to this thesis. Many thanks to Jeff and Brad, who helped me design, build and carry out these experiments. Thanks to ‘Wonderful’ Sean and George for help with the writing. Thanks should also go out to Ben and Graeme for their sage-like advice, which I hope I have put to good use.

I would like to thank all my friends who have provided me with welcome distractions, pot-lucks and good times. In particular, I would like to thank Vanessa for the encouragement, company and cooking adventures. Thanks also to my dear friends back home or away (they know who they are).

I must also gratefully acknowledge the financial and technical support I received from Rolls-Royce Canada and the Auto21 project.

Finally, I would like to thank my family, who I am sure will be very happy to have me home soon.

## ABSTRACT

The significant efforts to reduce global fossil fuel dependence have led to the development of biofuels as an alternative. Despite their growing significance, alcohol biofuels still require fundamental study, particularly in the area of  $\text{NO}_x$  emissions. Planar laser-induced fluorescence (PLIF) was used to obtain nitric oxide (NO) production profiles from stagnation flames of premixed *n*- and *iso*-butanol; *n*- and *iso*-butane flames were also measured to offer context with alkane fuels. PLIF measurements were corrected for laser sheet variations and non-radiative quenching by signal post-processing and quantified with a NO-seeding calibration method. Particle-image velocimetry (PIV) was performed to characterize the centreline velocity of the experimental flow which was then used for chemical kinetic simulations of the experiment. Simulations were performed for *n*-butanol and *n*-butane flames with a combined  $\text{NO}_x$  submechanism.

Experimentally, butanol fuels were found to produce significantly less NO than butane fuels overall. Although both models accurately predict the production of NO in the post-flame region, there is a disparity in NO production occurring in the flame zone via the prompt-NO pathway, suggesting that the chemical kinetics in the mechanisms require modification. The *n*-butanol simulation shows poor agreement at all tested equivalence ratios, while *n*-butane performed poorly for the rich case. This study offers new experimental data to aid in further improvements in kinetic modelling of butanol and butane combustion, and  $\text{NO}_x$  formation.

## ABRÉGÉ

Les efforts significatifs pour réduire la dépendance globale aux hydrocarbures ont entraîné le développement de biocarburants comme alternative. Malgré leur importance accrue, les biocarburants à base d'alcool nécessitent toujours une étude fondamentale, particulièrement en ce qui à trait aux émissions d'oxydes d'azote ( $\text{NO}_x$ ). La fluorescence planaire induite par un laser (PLIF) est utilisée pour obtenir les profils de production d'oxyde nitrique (NO) à partir de flammes de stagnation prémélangées de *n*- et *iso*-butanol ainsi que de *n*- et *iso*-butane pour mettre en contexte les carburants alcalins. Les mesures PLIF sont corrigées par un traitement ultérieur et quantifiées par une méthode de calibration. La vélocimétrie particule-image (PIV) est utilisée pour caractériser la vitesse de la ligne-médiane de l'écoulement expérimental qui est ensuite utilisée pour les simulations de cinétique chimique de la flamme expérimentale. Les simulations sont générées pour les flammes de *n*-butanol et de *n*-butane et sont combinées à un sous-mécanisme pour le  $\text{NO}_x$ .

Même si les deux modèles semblent bien prédire la production de NO dans la région après-flamme, il existe une disparité dans la production de NO dans la région de la flamme, ce qui suggère que les mécanismes cinétiques-chimiques requièrent amélioration. Le *n*-butanol démontre un piètre accord pour tous les ratios d'équivalence testés. Le *n*-butane, pour sa part, est imprécis pour le cas riche. Cette étude fournit de nouvelles données expérimentales qui aident à l'amélioration des modèles cinétiques-chimiques du butanol et du butane. Cette étude tend aussi à valider le sous-mécanisme du  $\text{NO}_x$  pour des combustibles à chaînes plus longues.

## TABLE OF CONTENTS

ACKNOWLEDGEMENTS . . . . .	iii
ABSTRACT . . . . .	iv
ABRÉGÉ . . . . .	v
LIST OF TABLES . . . . .	ix
LIST OF FIGURES . . . . .	x
1 Introduction and Literature Review . . . . .	1
1.1 Motivation . . . . .	1
1.2 NO Emissions . . . . .	3
1.3 Previous Studies of Butanol and NO <sub>x</sub> . . . . .	5
1.4 Research Focus . . . . .	10
2 Laser-induced Fluorescence . . . . .	12
2.1 Measurement Methods . . . . .	12
2.2 Laser-induced Fluorescence . . . . .	13
2.2.1 Planar Laser-Induced Fluorescence . . . . .	17
2.3 Nitric Oxide detection by PLIF/LIF . . . . .	19
3 Experimental Set-up and Methods . . . . .	24
3.1 Experimental Set-up . . . . .	24
3.1.1 Stagnation Flame Burner . . . . .	24
3.1.2 Flow Control and Liquid Fuel Delivery . . . . .	27
3.1.3 Data Acquisition and Control . . . . .	28
3.1.4 Flow field measurement - Particle Image Velocimetry . . . . .	29
3.1.5 Nitric oxide concentration measurements - Planar Laser-induced Fluorescence . . . . .	30
3.1.6 UV Optics and Signal Collection . . . . .	32

3.2	Experimental Procedure - Obtaining Measurements . . . . .	35
3.2.1	Heating and flow temperature . . . . .	36
3.2.2	Laser power measurements . . . . .	36
3.2.3	Excitation scan and wavelength check . . . . .	37
3.2.4	Stagnation Flames . . . . .	39
3.2.5	PIV Measurement Method . . . . .	40
3.2.6	NO-PLIF Measurement Methodology . . . . .	42
3.3	NO Profile Simulations . . . . .	45
3.3.1	Model and Mechanisms . . . . .	45
3.3.2	Initial Conditions . . . . .	46
4	PLIF Signal Post-processing . . . . .	48
4.1	Background Subtraction . . . . .	48
4.2	Simplifying the Problem . . . . .	48
4.3	Normalization by Laser Sheet Intensity - Run 1 . . . . .	49
4.4	Calibration Technique through constant NO seeding - Run 2 . . . . .	52
4.5	Measurement of Unseeded Flames - Run 3 . . . . .	58
4.6	Applying the calibration . . . . .	61
5	Results and Discussion . . . . .	64
5.1	Stagnation Flame Velocity and Reactivity . . . . .	64
5.1.1	Experimental Stagnation Flame Velocity Profiles . . . . .	64
5.1.2	Velocity Profile Comparisons to Simulation . . . . .	65
5.2	NO Production in Stagnation Flames . . . . .	70
5.2.1	Calibration Curves . . . . .	70
5.2.2	Experimental NO profiles for Butanol and Butane Flames . . . . .	74
5.2.3	NO Concentration Profile Comparisons . . . . .	80
5.2.4	Standard Deviation . . . . .	82
6	Conclusions . . . . .	86
	Appendix A: Obtaining Spatial PLIF Measurements . . . . .	89
	Appendix B: Maintenance and Continued Operation of the PLIF/Stagnation Flame System . . . . .	94
	Appendix C: NO Seeding Settings . . . . .	97
	Appendix D: Manipulation of Chemical Kinetic Mechanisms . . . . .	98

Appendix E: Boundary Conditions for Simulation . . . . . 100  
Appendix F: Quenching Corrections . . . . . 101  
Appendix G: Recommendations . . . . . 103  
References . . . . . 105

## LIST OF TABLES

<u>Table</u>	<u>page</u>
3-1 Runs performed for NO-PLIF measurements for each fuel case . . . .	42
5-1 Experimental $S_{u,ref}$ compared to simulations . . . . .	69
6-1 NO Seeding Flows . . . . .	97
6-2 Boundary Conditions input into Chemkin simulations . . . . .	100
6-3 Parameters generated by Chemkin simulations for quenching corrections and calculated correction factor . . . . .	102

## LIST OF FIGURES

<u>Figure</u>	<u>page</u>
1-1 Isomers of butanol . . . . .	6
1-2 Isomers of butane . . . . .	6
2-1 LIF electronic transitions . . . . .	15
2-2 Two-level theoretical model of LIF . . . . .	16
2-3 Fluorescence signal collection in PLIF . . . . .	16
2-4 Calibration curve for $\phi=0.7$ , $\text{CH}_4/\text{O}_2/\text{N}_2$ flame at 1 atm. Taken from Thomsen et al. [58] . . . . .	22
3-1 The stagnation flame experiment detailing the experimental geometry and the flow delivery system. . . . .	26
3-2 Particle image velocimetry (PIV) experimental optics configuration. . . . .	31
3-3 Simulated excitation scan of NO-LIF around 226 nm by LIFsim. . . . .	33
3-4 The UV optics arrangement and PLIF signal collection set-up. . . . .	34
3-5 Simulated excitation scan marked with 226.035 nm peak transition (on-line) and 226.048 nm minimum (off-line). . . . .	38
3-6 A <i>n</i> -butanol flame, $\phi = 1.0$ , seen with the corresponding centreline axial velocity plot. . . . .	41
3-7 Top: Stagnation flame with overlaid spatial $y$ -axis. Left: A single raw image of NO-PLIF in the shaded zone. The spatial coordinate ( $y$ - axis) is flipped due to the spherical collection lens. Right: NO-PLIF averaged over 500 images after background subtraction. . . . .	44
4-1 Normalized beam distribution functions for all fuels measured with a constant seeding of 45 ppm. . . . .	51

4-2	Raw calibration signals: <i>n</i> -butanol flame $\phi=0.8$ seeded with 28 ppm (blue) and 45 ppm NO (red). . . . .	53
4-3	Correlated calibration signals with beam non-uniformity removed: <i>n</i> -butanol $\phi=0.8$ flame seeded with 28 ppm (blue) and 45 ppm NO (red). . . . .	55
4-4	<i>n</i> -butanol calibration flame $\phi = 0.8$ , seeded with 28 ppm (blue) and 45 ppm (red). Uncorrected (dot), corrected ( $\nabla$ ) with averaged post-flame values (dash). Lean $\phi = 0.8$ native NO ( $\square$ ). . . . .	56
4-5	Calibration curve generated using averaged post-flame corrected signal: <i>n</i> -butanol $\phi=0.8$ calibration flame seeded with 28 ppm and 45 ppm. . . . .	58
4-6	Comparison of NO concentration profiles for $\phi=1.0$ <i>n</i> -butanol ( $\circ$ ) with quenching corrections (blue) and without quenching corrections(black)	61
4-7	NO-PLIF signals from unseeded <i>n</i> -butanol flames $\phi = 0.8$ ( $\square$ ), 1.0 ( $\circ$ ), 1.3 ( $\triangle$ ) . . . . .	62
4-8	<i>n</i> -butanol flame $\phi=1.0$ with the corresponding NO concentration plot, illustrating the spatial <i>y</i> -coordinate. . . . .	63
5-1	Centreline velocity profiles of <i>n</i> -butanol flames: $\phi=0.8$ (blue), $\phi=1.0$ (black), $\phi=1.3$ (red) . . . . .	65
5-2	Centreline velocity profiles of <i>iso</i> -butanol flames: $\phi=0.8$ (blue), $\phi=1.0$ (black), $\phi=1.3$ (red) . . . . .	66
5-3	Centreline velocity profiles of <i>n</i> -butane flames: $\phi=0.8$ (blue), $\phi=1.0$ (black), $\phi=1.3$ (red) . . . . .	66
5-4	Centreline velocity profiles of <i>iso</i> -butane flames: $\phi=0.8$ (blue), $\phi=1.0$ (black), $\phi=1.3$ (red) . . . . .	67
5-5	Photo of <i>n</i> -butanol (left) and <i>n</i> -butane (right) stagnation flames: $\phi=0.8$ (top), $\phi=1.0$ (middle), $\phi=1.3$ (bottom) . . . . .	68
5-6	Comparison of centreline velocity profiles (dots) to simulations (lines): $\phi=0.8$ (blue), $\phi=1.0$ (black), $\phi=1.3$ (red) . . . . .	71

5-7	Calibration curves for the four fuels: linear interpolation (line) of calibration points (●) . . . . .	72
5-8	Comparison of calibration curves: <i>n</i> -butanol (solid), <i>iso</i> -butanol (dash), <i>n</i> -butane (dot), <i>iso</i> -butane (dash-dot) . . . . .	73
5-9	NO concentration profiles for the four fuels: $\phi=0.8$ (blue), $\phi=1.0$ (black), $\phi=1.3$ (red) . . . . .	76
5-10	NO concentration profiles plotted separately as a function of equivalence ratio: <i>n</i> -butanol (blue ○), <i>iso</i> -butanol (teal □), <i>n</i> -butane (red ▽) and <i>iso</i> -butane (orange ◇) . . . . .	78
5-11	Comparison of NO concentration profiles to simulations: <i>n</i> -butanol (blue ○) with Sarathy-Dagaut mechanism (solid) and <i>n</i> -butane (red ▽) with USC_Mech V.II (dash) . . . . .	81
5-12	Standard deviation of <i>n</i> -butanol flames: $\phi=0.8$ (blue), $\phi=1.0$ (black), $\phi=1.3$ (red) . . . . .	85
6-1	An image of the focusing for to determine scale factor, averaged for 500 images. . . . .	90
6-2	Detailed dimensions and settings of the collection optics . . . . .	91
6-3	Vertical profile of fluorescence - test of magnification. Flow was seeded with NO molecules and excited at pre-defined points. . . . .	92
6-4	Magnification test plotted at 50% maximum. . . . .	93

## CHAPTER 1

### Introduction and Literature Review

#### 1.1 Motivation

Combustion of hydrocarbon fuel has been an essential part of industrialized human existence for over a century. Research in biofuel combustion is rapidly growing in importance as the global community attempts to reduce its dependence on fossil fuels for transportation and power. The development of new sources of fuel is necessary to match the increases in global energy consumption, which has been projected to increase 59% between 1999 and 2020 [12]. Much of this increase will be in the developing world, where many nations are without oil reserves or the resources to import fossil fuels, thus necessitating a need to look for alternatives [65]. The recent development of flexible-fuel vehicles demonstrates the growing importance of ethanol-blended fuels and other alcohol-based biofuels in Canada and internationally [34]. Alcohol biofuels like butanol can typically be produced from locally available and renewable natural resources such as corn, sugarcane or biomass feedstocks [17]. Despite the possibility of offering viable alternatives, the pollutant products from biofuel combustion still require study to determine any benefits over conventional fuels.

The environmental effects of the by-products of incomplete combustion have become a worldwide concern. While the primary products of combustion are carbon

dioxide and water, other harmful by-products are also produced like carbon monoxide, volatile organic compounds and oxides of nitrogen ( $\text{NO}_x$ ). The main oxides of nitrogen emitted to the atmosphere by combustion are nitric oxide ( $\text{NO}$ ) and nitrogen dioxide ( $\text{NO}_2$ ). While occurring naturally in small amounts,  $\text{NO}_x$  emissions have increased considerably due to the widespread combustion of fossil fuels. According to Bowman [11], global  $\text{NO}_x$  emissions from combustion sources have increased by a factor of ten since 1900. As developing countries continue to grow, the global demand for energy to support further economic development will inevitably lead to the continued rise in  $\text{NO}_x$  emissions. Transportation and power generation are the two dominant contributors of global  $\text{NO}_x$  emissions, contributing over 60% of total  $\text{NO}_x$  emissions in both North American and Asia [12].

There are significant health and environmental risks due to  $\text{NO}_x$  emissions, particularly in urban areas. Concentrated regions of  $\text{NO}_x$  release are known to be a significant cause of photochemical smog, acid rain and ground-layer ozone while depleting the upper ozone layer [56]. High concentrations of  $\text{NO}_x$  can also lead to several respiratory and cardiovascular health problems in humans. In North America and Europe, stringent emission laws have been passed by government agencies to reduce  $\text{NO}_x$ . While this has been successful in the last decade at lowering production trends in those regions, the rapid industrialization and commercialization of the developing world is projected to lead to increased  $\text{NO}_x$  emissions globally. It is projected that Asian  $\text{NO}_x$  emissions will continue to increase without slowing and is expected to double between 2000 and 2030 [29]. These trends illustrate the necessity of studying  $\text{NO}_x$  formation from combustive sources. The study of  $\text{NO}$  production in proposed

alternative fuels such as butanol will aid in the selection of suitable replacements for fossil fuel in the future.

## 1.2 NO Emissions

Nitric oxide, NO, is the primary NO<sub>x</sub> molecule emitted through combustion and is generally thought to be generated directly by three primary combustion pathways [11] - the thermal-NO, the fuel-bound nitrogen and the prompt-NO pathway. A fourth, the N<sub>2</sub>O-intermediate, is frequently mentioned as a separate pathway [59] although it was considered by Bowman [11] as part of the prompt-NO pathway.

The thermal-NO pathway results from the oxidation of atmospheric nitrogen with oxygen and hydroxyl radicals. NO formation is dependent on the burned-gas temperature due to the high activation energy of the rate-determining reaction  $O+N_2 \rightleftharpoons NO+N$ . Since the rate of thermal-NO formation is generally slow compared to fuel oxidation reactions, Miller and Bowman [38] conclude that the thermal mechanism can be decoupled from the fuel oxidation process. This pathway is known to be the primary contributor to NO production in aircraft and auto engines.

The fuel-bound nitrogen mechanism is a primary source of nitrogen oxide production for fuels such as coal, which contain chemically bound nitrogen. Generation of NO emissions with this mechanism can be minimized by selecting fuels with no fuel-bound nitrogen molecules.

The prompt mechanism, discovered by Fenimore [21], describes the fast reaction of hydrocarbon radicals with molecular nitrogen within the flame zone, leading to formation of amines or hydrocyanic acid (HCN) which then react to form NO. While the initially proposed primary path of the prompt mechanism was  $CH+N_2 \rightleftharpoons HCN+N$ ,

recent studies have shown that  $\text{CH} + \text{N}_2 \rightleftharpoons \text{NCN} + \text{H}$  is more likely as the primary path at high temperatures [39]. It has been found that NCN quickly reacts to form HCN as an intermediate, which then reacts further to generate NO. Several subsequent studies as described by Konnov [31] and Vovelle et al. [61] were performed to better determine the reaction rate constants for NO production and further improve and develop computational models that describe NO production.

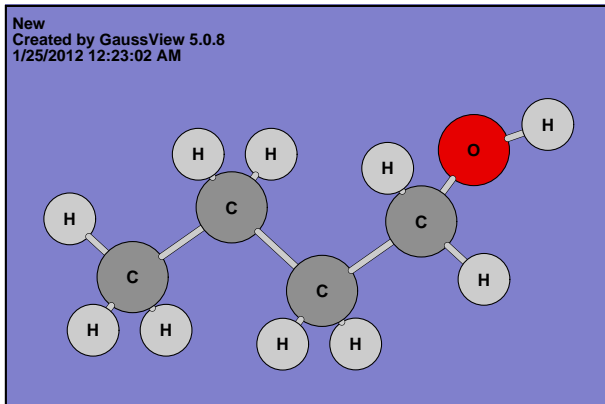
It has been concluded by several studies [20, 42] that the formation of prompt-NO is dominated by the aforementioned reaction steps and that the effects of other NO production pathways (such as through  $\text{N}_2\text{O}$  and NNH) for flames are negligible. Turns [59] notes that the  $\text{N}_2\text{O}$  pathway plays a larger role in NO production at very lean, low temperature or high pressure conditions. It should also be noted that there is a minor effect from the  $\text{NO}_2$  removal pathway, which converts NO to  $\text{NO}_2$ , however NO conversion will be very low at flame conditions.

NO is formed during the combustion of all types of hydrocarbon fuels - fossil and biofuel. The need to understand and model its formation is the subject of ongoing research. Most of the research with NO production has been performed with methane flames in different experimental configurations [3, 32, 41, 42]. The reduction of  $\text{NO}_x$  emissions will be essential for the continued viability of alcohol-based fuels such as ethanol and butanol in the future. Increasing the current knowledge of the chemical kinetics behind NO emissions in combustion is key to understanding and selecting future candidate fuels.

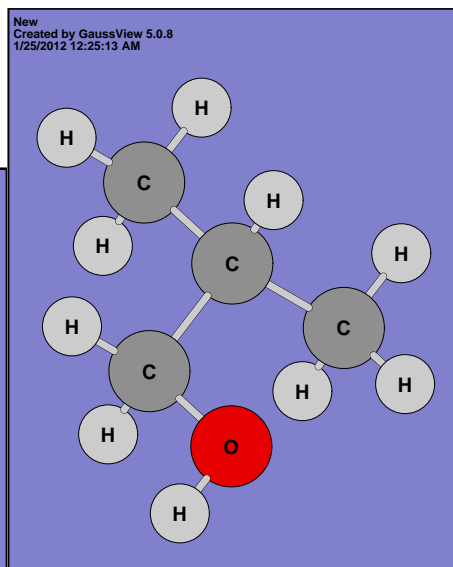
### 1.3 Previous Studies of Butanol and NO<sub>x</sub>

Butanol (C<sub>4</sub>H<sub>9</sub>OH) is an alcohol biofuel which consists of a chain of four carbon atoms bonded to a hydroxyl group. The use of butanol instead of ethanol as a fuel or fuel additive could be favourable in several ways: it has a higher energy density leading to better fuel economy, lower vapour pressure thus reducing the chance of explosion, and better resistance to water contamination [40]. There are four isomers of butanol – *n*-butanol (also known as 1-butanol), *sec*-butanol (2-butanol), *iso*-butanol and *tert*-butanol – all with different combustion characteristics, intermediates and products [37]. *n*-Butanol, Fig. 1–1a, and *iso*-butanol, Fig. 1–1b, are the most reactive butanol isomers [40] and are more suited for use as fuel additives or neat fuels. Due to its favourable characteristics and the recent commercialization of its production, butanol has been the subject of significant research to characterize its combustion. Butanol flame speeds [25, 60], intermediate products [37, 43, 64] and ignition delays [40] have been investigated in several studies.

The study of butanol combustion can be better approached by putting it in the context of the combustion of a similar fossil fuel, such as butane. Butane (C<sub>4</sub>H<sub>10</sub>) is a four-carbon alkane fuel with two isomers - *n*-butane, Fig. 1–2a, and *iso*-butane, Fig. 1–2b. Butane is easily liquefied and frequently used as lighter or camp fuel. Compared to butanol, it has a slightly higher adiabatic flame temperature. The two isomers of butane were selected for comparative study against the two corresponding isomers of butanol. The relative production of NO<sub>x</sub> in butane flames is of particular interest as a comparison to butanol flames – with this comparison, there can be an analogy made to alcohol and alkane fuels in general.

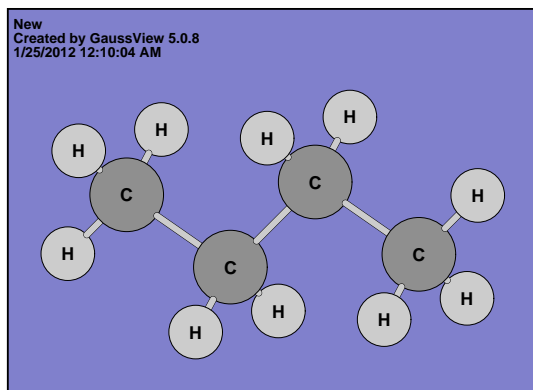


(a) nbutanol

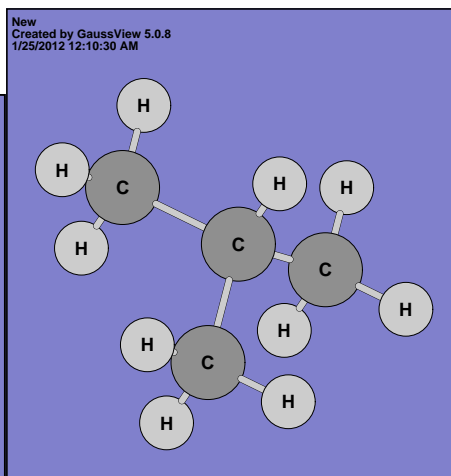


(b) isobutanol

Figure 1-1: Isomers of butanol



(a) nbutane



(b) isobutane

Figure 1-2: Isomers of butane

Despite their growing significance today, alcohol fuels still require fundamental study, particularly in the area of  $\text{NO}_x$  emissions. To date, there have been several studies measuring the effect of alcohol-blended gasoline on  $\text{NO}_x$  emission in automotive engines [44, 63, 65]. The results from these studies have been mixed, showing an improvement in  $\text{NO}_x$  emissions for certain cases and blends. Despite general interest with  $\text{NO}_x$  emissions from alcohol fuels within the auto industry, there has been a dearth in corresponding fundamental research that is free of engine-related complications like spark timing or fuel spray. Flame experiments offer a simplified platform on which NO formation due to fuel effects can be separated from other confounding factors thus providing accurate measurements and targets for kinetic modelling.

Models play a large role in furthering our understanding of the chemistry behind combustion and pollutant formation. A chemical kinetic model is a computational model which describes the complex chemical processes that occur during combustion. Knowledge of the chemical pathways, the paths through which reactant species are transformed into product species, is critical to truly understanding the combustion of fuels and creation of the resulting products.

A  $\text{NO}_x$  sub-mechanism, for example, is a computational model which describes the various mechanisms of NO production and the chemistry occurring during a combustion reaction. The experimental verification of a model is essential to determine its validity; only through a rigorous comparison between computational and experimental results can one be convinced of the accuracy of these models.

Mechanisms can be validated by the measurement of experimental quantities such as species concentration or flame propagation speed - these quantities can either be compared directly to the simulation, or be manipulated mathematically and compared to other simulated quantities. Measurement of the profile and concentration of intermediate or product species in the combustion and post-flame zone is very useful in model validation. Making measurements of species profiles will allow researchers to determine the dominant pathways in which fuel is consumed. The experimental species production or consumption profiles can be compared to those simulated through a chemical kinetic model. A discrepancy between these profiles could indicate that an improvement of the model is necessary. NO concentration profiles of butanol flames can be measured experimentally through spectroscopy, which can then be compared to simulated profiles with the appropriate kinetic mechanisms.

Several models were considered as candidates for experimental verification. These models contain detailed kinetic reactions for the combustion of the candidate fuels, which should accurately capture intermediate species production. In most cases, these models do not contain reactions that describe formation of NO<sub>x</sub> species, requiring the addition of a NO<sub>x</sub> sub-mechanism into the base mechanism.

There are several models which have been designed for hydrocarbon combustion up to and including butane: USC\_Mech Version II of C1-C4 mechanism [62] from USC and C1-C5 mechanism [26, 27] from NUI Galway were considered. USC\_Mech was selected because of its computational ease-of-use and its extensive validation for both laminar flame speeds and burner stabilized flames. It consists of 111 species and 784 reactions.

Despite its recent emergence as an alternative fuel, there are several mechanisms available for isomeric butanol combustion [24, 40], although they generally lack the amount of experimental validation of more established alkane reaction mechanisms. While lacking reactions for *iso*-butanol, the mechanism by Sarathy et al.[17, 51] was selected because it appears to be well validated for laminar and non-premixed *n*-butanol flames. The Sarathy-Dagaut mechanism consists of 117 species and 884 reactions

The modelling of NO<sub>x</sub> reactions is a very active field of study, with multiple available sub-mechanisms validated through a variety of methods. The Konnov mechanism [16, 30, 31] and GDF\_kin3.0 [20, 32] mechanism both featured detailed chemistry of prompt-NO formation, as well as experimental validation with flames. The UIC-Dagaut mechanism [55] is a mechanism validated with flow reactor and shock tube experiments. Ultimately, GDF\_kin3.0 was selected as it emphasized prompt-NO formation and was smaller than the others (121 species/883 reactions) and therefore easier to combine with the base mechanism.

Marques et al. [35] studied NO production of atmospheric pressure ethanol flames using laser-saturated fluorescence (LSF) and chemiluminescence and compared production profiles to simulations. The obtained LSF data indicated that the thermal-NO mechanism was dominant in stoichiometric ethanol flames and the prompt-NO mechanism was dominant in rich flames. The experimental results of NO production were compared to an ethanol mechanism [36] – good agreement was found between stoichiometric and slightly rich flames, although very rich flames showed poor agreement.

Lamoureux et al. [32] recently used LIF to measure NO concentrations in low pressure laminar CH<sub>4</sub>/O<sub>2</sub>/N<sub>2</sub> flames containing varying amounts of methyl-ethyl ketone (MEK) and ethyl acetate (EA). A sub-mechanism containing MEK and EA chemistry was added to GDF\_kin3.0 [20]. A conclusion reached by detailed pathway analysis of NO formation was that the oxygenates typically produce less NO than methane because there are fewer CH radicals produced in the flame leading to less prompt-NO formation.

Both papers provided valuable insight into NO production in oxygenated flames, while also providing validation for the tested chemical kinetic models.

#### 1.4 Research Focus

Within this study, an apparatus was built to measure the concentration of nitric oxide using planar laser-induced fluorescence (PLIF). PLIF is a spectroscopic method that involves the excitation of nitric oxide by a laser sheet, followed by the detection of the resulting fluorescence. The development and construction of this apparatus, based on cited works, was carried out for the purposes of this thesis. Isomeric butanol and butane stagnation flames were tested at three equivalence ratios,  $\phi = 0.8, 1.0$  and  $1.3$ . NO-PLIF profile measurements were corrected for laser sheet variations and non-radiative quenching by signal post-processing and quantified with an NO-seeding calibration method. Using velocity field information obtained through particle image velocimetry (PIV), chemical kinetic simulations were performed for NO production of *n*-butanol and *n*-butane within the stagnation flame geometry. The techniques used for performing PIV were developed by previous laboratory co-workers [22, 50]. The production profiles between experiments and simulations were

compared and analysed. This thesis will contribute experimental data consisting of quantitative nitric oxide concentrations of previously unmeasured *n*-butanol and *iso*-butanol flames. Within the context of air pollution, the differences in NO production between alcohols and alkanes will be investigated to determine the suitability of using butanol as an alternative to current fossil fuels. This study endeavours to further aid the modelling and understanding of butanol and butane combustion, particularly with respect to NO<sub>x</sub> formation.

## CHAPTER 2 Laser-induced Fluorescence

### 2.1 Measurement Methods

A variety of experimental set-ups can be used for validation of kinetic models - for equilibrium or steady-state simulations such as a perfectly-stirred reactor, studies are performed using flow reactors or jet-stirred reactors. To validate a mechanism for flames, experiments with burner-stabilized flames, diffusion flames, stagnation flames and constant-volume bombs can be used.

Depending on the desired experimental quantity of study and the experimental apparatus, there are multitude of measurement methods available. To obtain laminar flame speeds, researchers have employed several optical methods such as particle streak velocimetry [4, 5] or schlieren photography [25, 51]. Particle image velocimetry (PIV) has also been demonstrated to be an excellent method for the measurement of a two-dimensional flow field in a laminar stagnation flame from which laminar flame speed can be extracted [22, 50, 60].

Nitric oxide emissions from flame experiments have generally been measured either optically using an optical measurement method, or using a probe sampling method. While there are several advantages to using a sampling method, such as the ability to detect intermediate combustion species and a lower species detection limit, it is an intrusive method and could impact the location and properties of the flame [49]. Furthermore, it is possible that decomposition reactions could occur within the

probe before the sampled gas could be analysed [31]. Optical methods, however, were found to be preferable as they do not affect the flame during measurement and species measurements can be obtained quickly as compared to the sampling method.

## 2.2 Laser-induced Fluorescence

Optical measurement methods have been developed over the last decade to the point where they can quantitatively measure the concentration of NO within the flame. Laser saturated fluorescence (LSF) and, more recently, laser-induced fluorescence (LIF) have been used extensively for these measurements. Planar laser-induced fluorescence (PLIF) involves the manipulation of a laser pulse to form a thin sheet of light using an array of optics which is then directed at the flame zone. The wavelength of the laser is chosen to be resonant with an optical transition of a species (in this case, NO) present in the flow such that a fraction of the incident laser light is absorbed at each point in the illumination plane. The absorbed photons are then re-emitted at several other characteristic wavelengths through fluorescence. The emitted light is then collected, focused, spectrally filtered and detected through various means.

LIF usually involves a linear excitation range - the fluorescence signal output is proportional to the excitation power of the laser. While LSF operates using generally the same principals as LIF, it involves exciting with significantly more laser power. This saturation takes the resulting signal out of the linear range, making it relatively independent of laser irradiance while also significantly increasing noise. Compared to LSF, LIF features a superior signal-to-noise ratio which allows for the observation of species at low concentration while reducing background signal [48, 53]. Recent

research has focused on the benefits of using planar laser-induced fluorescence as an alternative to LSF measurements. Cooper et al. [15] and Ravikrishna et al. [46] described the implementation of quantitative LIF and PLIF measurements as compared to LSF, demonstrating the ability of all three methods to measure quantitative NO concentrations.

Fig. 2-1 describes the excitation of a molecule to an excited electronic state through absorption of a photon, followed by some amount of radiationless decay of energy. When the molecule returns to its ground electronic state, a photon is re-emitted at several discrete wavelengths corresponding to its excited and ground rovibrational state. Thus, for a larger population of excited molecules, a spectrum of the resulting fluorescence can be detected by instrumentation and then imaged. Although unshifted fluorescence – fluorescence at the same wavelength as excitation – does occur, measurement of spectrally shifted fluorescence is preferable to avoid mixing signals with scattered laser light and Rayleigh/Mie scattering occurring at the excitation wavelength.

Applied generally for LIF or PLIF, the collected fluorescence signal can be written as a function of several terms pertaining to both experimental and theoretical variables. Measurement or calculation of these variables will yield a resulting fluorescence signal corresponding to the concentration of the ground-state population of NO molecules within the area of interest.

One can consider the excitation of species and re-emission of light in a two-level framework and thus develop equations and terms to describe associated rates. The two-level model seen in Fig. 2-2 describes the radiative transitions between a lower

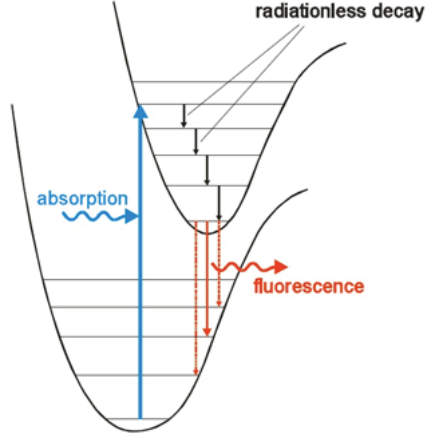


Figure 2-1: LIF electronic transitions

and upper electronic energy state. Adopting notation primarily from Laurendeau [33], an equation describing the transitions between upper and lower level population can be written as:

$$\begin{aligned}\frac{\partial n_l}{\partial t} &= n_u A_{ul} - n_l B_{lu} \rho_\nu + n_l B_{ul} \rho_\nu + Q_{ul} n_u \\ \frac{\partial n_u}{\partial t} &= -n_u A_{ul} + n_l B_{lu} \rho_\nu - n_l B_{ul} \rho_\nu - Q_{ul} n_u\end{aligned}$$

Number densities of the lower and upper states are  $n_l$  and  $n_u$ , respectively.  $A_{ul}$  ( $s^{-1}$ ) is the Einstein coefficient for spontaneous emission and the first term in both equations.  $A_{ul}$  ( $s^{-1}$ ) describes the rate of spontaneous emission of energy from the upper to lower state. Similarly,  $B_{ul}$  and  $B_{lu}$  ( $m^3/J \cdot s^{-1}$ ), the Einstein coefficients for stimulated emission and absorption, describe the rates of transitions of states for the second and third terms when multiplied by  $\rho_\nu$  ( $J/m^3 \cdot s^{-1}$ ), the radiative energy density at frequency  $\nu$ . Finally,  $Q_{ul}$  ( $s^{-1}$ ) describes the rate at which the upper

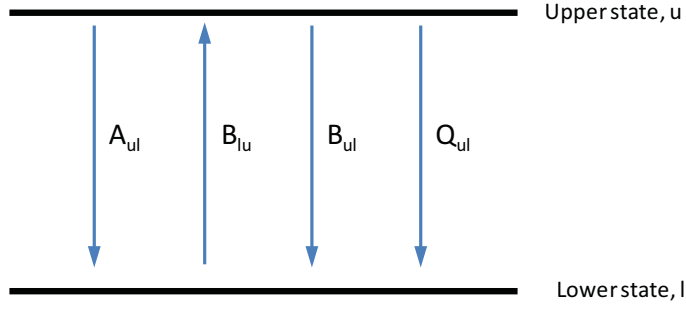


Figure 2-2: Two-level theoretical model of LIF

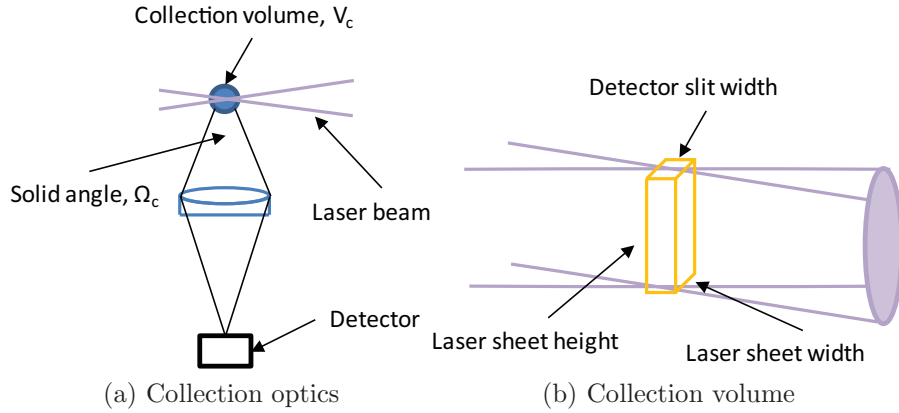


Figure 2-3: Fluorescence signal collection in PLIF

population transitions to lower due to non-radiative quenching from inter-molecular collisions experienced by the excited population.

It can be found that the experimentally-measured LIF signal,  $P_d$ , can be expressed as:

$$P_d = h\nu_{ul} \left( \frac{A_{ul}B_{ul}}{Q_{ul}} \right) \frac{\Omega_c}{4\pi} V_c n_l^\circ \rho_\nu \quad (2.1)$$

The derivation of this equation can be found in [33].

The fluorescence signal is found to be proportional to the initial lower state population,  $n_l^\circ$ , as well as the energy density of laser excitation,  $\rho_\nu$ . The first two

terms in the equation,  $h\nu_{ul}$  describe the energy change between levels due to the emission of a photon from the excited state. The quenching coefficient  $Q_{ul}$  is typically much larger than  $A_{ul}$  and  $B_{ul}$  and is a function of the pressure condition and of the collision species. The term  $\frac{\Omega_c}{4\pi}V_c$ , where  $V_c$  is the collection volume and  $\Omega_c$  is the optical collection term, describes the physical conditions of optical collection of the fluorescence (see Fig. 2–3a and Fig. 2–3b).

The fluorescence signal for planar LIF can also be calculated through the above equation while accounting for the additional spatial dependence of several of the terms.

### 2.2.1 Planar Laser-Induced Fluorescence

Using PLIF in an experimental flame geometry presents a distinct advantage over LIF. As LIF only measures the concentration of species at a specific excitation point, there would be a need to scan the beam or move the experiment in order to obtain a measurement of a species profile along a particular axis. PLIF allows for the spatial measurement of species concentration along a particular axis through a zone of interest. Fig. 2–3a shows a PLIF-type experimental set up, where an expanded circular beam is focused to form a light sheet through the collection volume,  $V_c$ . The sheet has a specified height equal to the diameter of the circular beam as seen in Fig. 2–3b.

PLIF can be subject to non-uniformity in beam sheet intensity, leading to a non-uniform excitation of molecules. However, if the method is used within the linear excitation regime, the resulting fluorescence signal can be linearly scaled to laser

power, so corrections can be made as long as the energy variation in the beam sheet is spatially known.

An expression for PLIF can be written as an adaptation of the previous LIF equation, Eq. 2.1. The PLIF equation will require the modification of several terms, which will vary with respect to spatial location (hereby denoted as the y-coordinate).

$$P_d(y) = h\nu_{ul} \left( \frac{A_{ul}B_{ul}}{Q_{ul}} \right) \frac{\Omega_c(y)}{4\pi} V_c n_i^\circ(y) \rho_\nu(y) \quad (2.2)$$

The term of primary interest is  $n_i^\circ(y)$ , which was previously described as the initial ground state population of the excited molecule.

$$n_i^\circ(y) = \chi_{[\text{NO}]}(y) \frac{N}{V}(y) \quad (2.3)$$

The ground state population of the NO is equal to the mole fraction of NO,  $\chi_{[\text{NO}]}(y)$ , multiplied by the number density of all molecules,  $\frac{N}{V}(y)$ . A flame stabilized within the bounds of the beam sheet will produce a certain mole fraction of NO due to the chemical reactions occurring within the flame or in the post-flame region. The change of NO production within the collection volume as a result of the flame will make  $\chi_{[\text{NO}]}(y)$  vary spatially. The expansion of gases through the flame also greatly reduces the number density,  $\frac{N}{V}(y)$  of all molecules, leading to a significant drop in  $n_i^\circ(y)$  and consequently,  $P_d(y)$ . Ultimately, the goal is to isolate  $n_i^\circ(y)$  as the only unknown in the equation, allowing for the determination of spatial concentration of NO molecules in the collection volume.

The optical collection term,  $\Omega_c(y)$ , is y-dependent due to aberrations and distortions in the optics, either in the collection lens or within the various mirrors and

gratings within the spectrograph. It is assumed that the laser sheet does not change in shape during the experiment, thus  $V_c$  is constant. In addition, the  $\rho_\nu(y)$  term, which represents the energy density of laser excitation, is  $y$ -dependent due to the non-uniformities in the excitation sheet:

$$\rho_\nu(y) = I_{\text{laser, total}} f(y) \quad (2.4)$$

In Eq. 2.4,  $\rho_\nu(y)$  is a product of the summed laser intensity and a function,  $f(y)$  describing the distribution of the energy across the bounds of the laser sheet.

The remaining terms,  $h\nu_{\text{ul}}(A_{\text{ul}}B_{\text{ul}})$  are generally constant given a constant temperature and pressure condition as they are primarily dependant on intrinsic molecular properties. However, the presence of a flame in the collection volume will also lead to a change in the collisional quenching term  $Q_{\text{ul}}$  because it is temperature and species dependent. Due to the difficulty in measuring  $Q_{\text{ul}}$  experimentally, a method is used in which these constant terms are inferred from previous research. This method will be discussed at length in Chapter 4.

### 2.3 Nitric Oxide detection by PLIF/LIF

PLIF or LIF spectroscopy of NO molecules requires precise calibration and experimental control for quantitative measurements. Various studies have been reported on spectroscopy of NO since the early 1990's, starting first with qualitative measurements but eventually developing techniques for quantitative measurements. Several studies have also investigated high pressure NO-LIF spectroscopy, allowing researchers to simulate conditions closer to those experienced in engines [19, 53].

The choice of excitation wavelength is of high importance for PLIF, particularly at high pressures – selection of a stronger NO excitation peak will yield higher fluorescence signals at the same beam power. The strength of the absorption line represents the intensity of the coupling between the excited and ground electronic states [1]. Poor excitation wavelength selection could lead to lower signal-to-noise ratios and significant O<sub>2</sub> interferences at high pressures due to the proximity of the NO(0,0) band to the Runge-Schumann O<sub>2</sub> bands.

Studies of NO-LIF excitation and detection are performed frequently at high pressures as the increasing amount of interference necessitates a greater focus on excitation strategies. Bessler et al. [7, 8, 9] published a series of papers detailing studies of excitation strategies within single vibrational levels A-X(0,0), A-X(0,1) and A-X(0,2) for a range of pressures between 1 and 100 bars. Under standard conditions, the largest total signal for NO fluorescence was obtained by exciting the A-X(0,0) band (near 225 nm) and detecting (0,1) and (0,2) (around 236 and 237 nm respectively). Signal interferences with NO from O<sub>2</sub>, CO<sub>2</sub> and polycyclic aromatic hydrocarbons were also investigated and found to not be significant for low pressure flames.

Bessler et al. [9] indicate that there are two electronic transitions that yield excellent results at atmospheric pressures and display low temperature sensitivity. The DiRosa transition and the Laurendeau transition were both found to yield strong signals at low pressures. The DiRosa transition was so-named by Bessler et al. [9] for high pressure studies performed by DiRosa et al. in 1996 [19]. The transition, which describes the NO feature P<sub>1</sub>(23.5), Q<sub>1</sub>+P<sub>21</sub>(14.5), Q<sub>2</sub>+R<sub>12</sub>(20.5), is found by

exciting at a wavelength of 226.034 nm and was originally proposed by Battles and Hanson [1]. The Laurendeau transition has been used extensively by researchers at Purdue University [13, 14, 15, 46, 45, 47, 58]. The transition describes the Q<sub>2</sub>(26.5) line feature found at 225.58 nm. While both excitation wavelengths offer excellent signal yields at atmospheric pressures, Bessler et al. found that the DiRosa excitation provided the maximum signal strength and minimized O<sub>2</sub> interferences at all pressures.

Corrections to account for O<sub>2</sub> interferences and ambient instrument noise are often necessary to improve the quality of the signal analysis. Both Thomsen et al. [57] and Cooper et al. [15] discuss background correction methods in detail. Selections were made for ideal on-line measurements, which provide strong fluorescence signals with low noise, and off-line measurements, which do not excite NO but provides a background similar to the on-line case. The background noise is collected when the excitation is tuned to an off-line wavelength (225.53 nm) – the signals detected over the range in this case will only be background excitation of OH or O<sub>2</sub> molecules and Mie scattering effects, since NO is not resonant at that wavelength. Thus, when the laser excites at the NO resonant 225.58 nm wavelength, the true NO fluorescence signal can be separated from the background through subtraction.

While planar laser-induced fluorescence can be used as an effective tool for imaging concentration fields, the measurements that can be made from the imaging are highly dependent on the experimental set-up. PLIF cannot inherently provide absolute number densities or concentrations of the detected molecule – a relative signal intensity can be detected along the imaged region, but a correlation must be

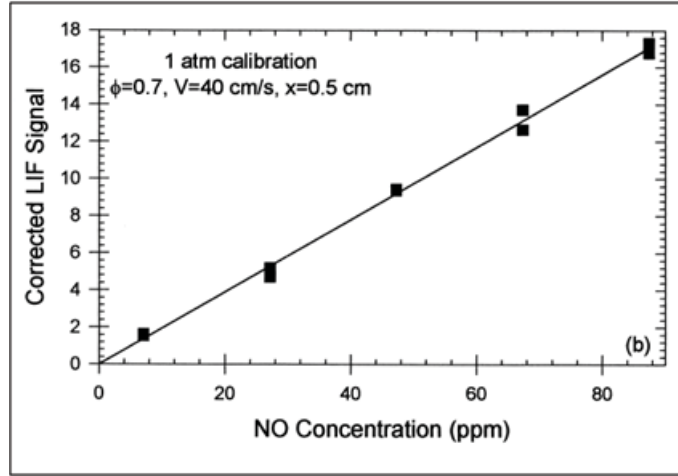


Figure 2-4: Calibration curve for  $\phi=0.7$ ,  $\text{CH}_4/\text{O}_2/\text{N}_2$  flame at 1 atm. Taken from Thomsen et al. [58]

made to relate this signal to an absolute number. Thus, in order to quantitatively measure concentrations of nitric oxide in a flame, a calibration method must be created which relates the detected fluorescence signal to a known concentration.

Frequently, a NO seeding calibration method is employed in NO-PLIF/LIF literature where quantitative concentration measurements are made. The general process of this seeding method is described in detail notably by Reisel et al. [48] and Thomsen et al. [57]. The goal of the calibration is to generate a linear plot in which a known NO concentration can be related to a corresponding fluorescence signal given constant experimental conditions. An example of a calibration curve can be seen in Fig. 2-4, taken from [58]. The calibration method will be discussed in detail in Section 4.4.

Nitric oxide re-burn becomes a consideration when the calibration method is applied. It describes the process in which existing NO molecules, such as those

seeded into a calibration flame, can be consumed in the combustion or flame zone. The unknown consumption of NO would yield a lower concentration of seeded NO in the post-flame region, thus affecting the quantitative accuracy of calibration - the calibration curve assumes that all seeded NO molecules are present pre- and post-flame.

Re-burn studies [3, 57] have used simulations to predict the re-burn rate of seeded NO. Although re-burn reactions become relevant at higher levels of seeding and with a richer calibration flame, it was found that small amounts of seeding lead to negligible amounts of re-burn. Indeed, at the lowest seeding condition tested by Berg et al. [3], 750 ppm of seeded NO in a  $\phi=0.8$  methane laminar calibration flame resulted in a predicted re-burn rate of 2%. Thomsen et al. [57] performed similar modelling of NO re-burn for a concentration of 250 ppm in a  $\phi=0.6$  methane opposed flow flame and found less than 5% NO destruction. Thus, for calibration curve generation, the maximum amount of experimentally seeded NO was kept below 250 ppm and an assumption was made that no seeded nitric oxide molecules were consumed through the flame.

## CHAPTER 3 Experimental Set-up and Methods

### 3.1 Experimental Set-up

#### 3.1.1 Stagnation Flame Burner

The stagnation flame experimental apparatus was used for the combustion of fuels and measurement of NO concentrations by PLIF. A stagnation flow is created by a laminar jet of premixed fuel and air, which is accelerated through a nozzle contraction, impinging on a steel, water-cooled stagnation plate. This impinging-jet geometry forces the axial flow to expand in a radial direction, creating a region of strained, steady-state flow. The flame which can be ignited within the stagnation flow is stable and steady - the centreline of this flame can be assumed to be 1-D and axisymmetric. Thus, this geometry is ideal for comparisons between experiment and simulation due to the steadiness of the flame, good knowledge of the boundary conditions (flow speed, flow temperature, stagnation plane temperature), and the relatively low computational cost involved in simulating a 1-D flow. The experimental geometry can be seen in Fig. 3-1 on the upper right.

The stagnation flame burner consists of a brass nozzle and a cylindrical bronze plenum which are screwed together into a base-plate. The heated steel supply pipe is connected to the bottom of the base-plate from below, directing premixed fuel and air into the plenum. The flow is kept laminar through the plenum by disrupting turbulent development by several means: using a diffuser at the plenum inlet, a

ceramic flow straightener, and several perforated screens. The flow is then accelerated through the brass contraction nozzle, exiting the burner in a laminar, top-hat profile. The contraction nozzle has an exit diameter of 20 mm. There is a secondary flow of nitrogen through the co-flow nozzle, which acts to sheath the inner premixed flow from the outside environment. The co-flow is similarly accelerated through a concentric outer contraction nozzle.

The premixed flow impinges on a stagnation plate held at a separation distance of 25 mm from the nozzle exit, which gives a L/D ratio of 1.25. The L/D ratio is sufficiently high to minimize the effect of the stagnation plate on the flow immediately exiting the nozzle - thus upon its exit from the contraction nozzle, the premixed fuel-air is moving at a velocity equal to its flow rate divided by the nozzle area  $V_{\text{exit}} = Q_{\text{flow}}/A_{\text{nozzle}}$  [4].

The nozzle-plenum assembly is also heated in a similar way to the supply pipes - a temperature controller controls heating tapes which are attached to the inner and outer bronze plena. The temperature of the nozzle is taken by a surface thermocouple on the outside wall of the nozzle. As the flow enters the plenum and exits through the nozzle, the temperature of the surrounding walls are maintained such that negligible cooling occurs in the flow. The stagnation plate is water-cooled and maintained at a constant temperature using a K-type thermocouple (Omega) embedded beneath the surface of the plate.

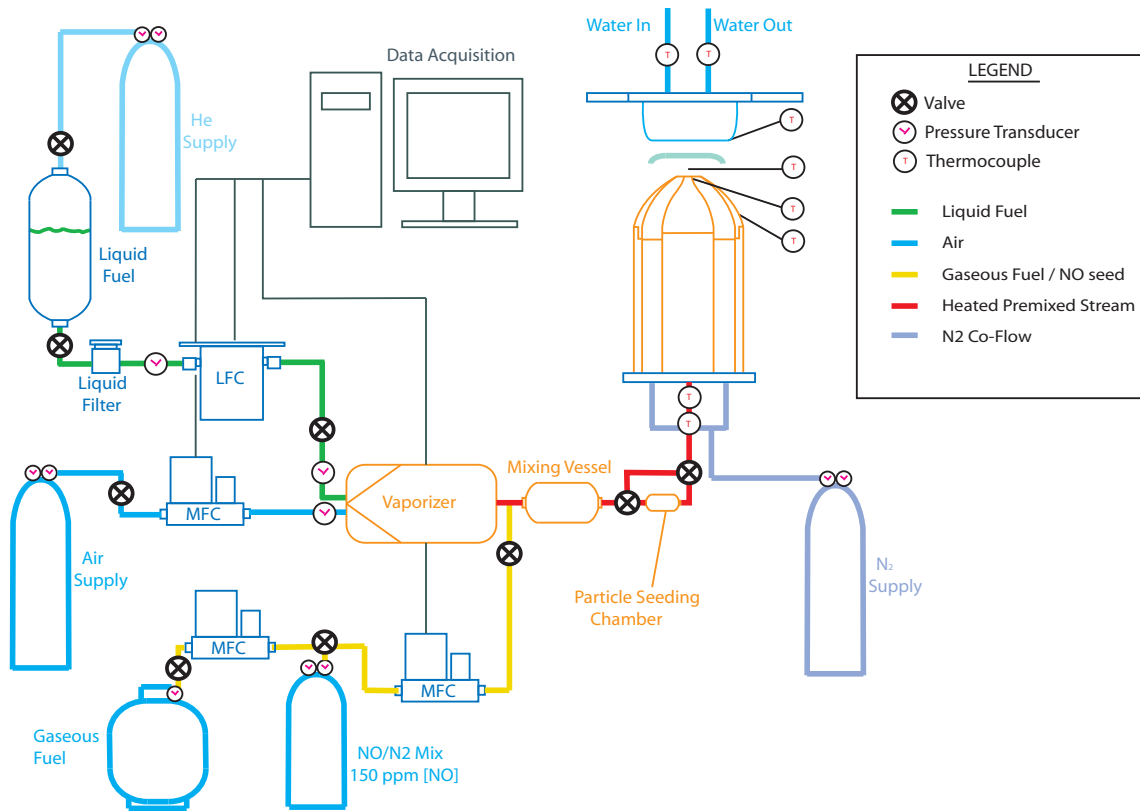


Figure 3-1: The stagnation flame experiment detailing the experimental geometry and the flow delivery system.

### 3.1.2 Flow Control and Liquid Fuel Delivery

Flame experiments require precise control of fuel and oxidizer flow in order to keep the equivalence ratio of the flame constant. A schematic of the flow control used in the experiment can be seen in Fig. 3-1.

Oxidizer and co-flow gases are supplied to the system using compressed gas cylinders, equipped with two-stage gas regulators. The flow of oxidizer (in most cases, air) is controlled by a Brooks Mass Flow Controller (100 SLPM, accurate to 0.2% of rate plus 0.7% of reading) -- the controller regulates the mass flow by measuring heat dissipation to determine and control the flow rate of air. The oxidizer stream is sent to the vaporizer to be mixed with liquid fuel. The nitrogen co-flow, used to sheath the premixed flame from the outside environment, is controlled by a needle valve and supplied to the outer plenum.

Liquid fuel is held in a stainless steel tank and kept under constant pressure (30 psi) by pressurized helium gas. When the valve is open, liquid fuel flows through the lines and is controlled and metered by a Brooks Coriolis Liquid Flowmeter (500 g/hr, accurate to 0.2% of rate). It is then vaporized into the heated air stream by a Brooks Vaporizer DLI 750 system. The vaporizer consists of two orifices and a heated chamber, in which liquid fuel is sprayed, vaporized and mixed with incoming air. The premixed fuel and air is then sent through heated stainless steel pipes to the nozzle-plenum assembly.

In the case of butane flames, another Brooks MFC (5 SLPM of  $\text{CH}_4$ ) is used to control the fuel flow. A third Brooks MFC (50 SLPM of air) is used when  $\text{NO}/\text{N}_2$  seeding is necessary.

Great care was taken to maintain a high enough temperature throughout the system to minimize the amount of fuel condensate. Temperatures are monitored immediately before the nozzle inlet and maintained at 95°C. The temperature of the vaporizer and heated pipes is set and monitored by in-flow thermocouples. Each thermocouple corresponds to its own temperature controller (Omega CSC32 Benchtop Controller) which maintains the temperatures of two fibreglass cloth heating tapes (Omegalux) which are wrapped around the stainless steel lines. The temperature immediately upstream of the plenum is taken by another in-flow thermocouple and recorded in a data acquisition system.

### **3.1.3 Data Acquisition and Control**

A data acquisition system is used to designate air and fuel flow setpoints as well as record and maintain temperatures within the system. The data acquisition hardware was supplied by National Instruments and the controlling software was written and implemented in NI-LabVIEW 8.5. The virtual instrument (VI) was previously created in-house and was modified to perform the tasks required to control the gas and liquid flow delivery systems. The user inputs to the VI include fuel type, flow temperature, desired equivalence ratio and desired nozzle exit velocity. The VI, given the conditions, then calculates and implements the necessary setpoints for the air and liquid flow controllers. The VI is also used to monitor relevant temperatures within the stagnation flame apparatus. Data from thermocouples measuring flow exit temperature, flow temperature upstream of the nozzle, and stagnation plate temperature is sent to the VI via the data acquisition system and recorded.

### 3.1.4 Flow field measurement - Particle Image Velocimetry

Particle-image velocimetry (PIV) is used to characterize the flow field within the stagnation flame geometry. Determining the centreline velocity of the flow is essential to determine several experimental variables needed for simulation. Through measurement of the flow field, it is possible to simulate the experimental geometry using a chemical kinetic simulation software such as Chemkin [18] or Cantera [23].

PIV is performed by imaging two instances separated by 110  $\mu\text{s}$  during which the flow field was illuminated by a laser sheet. Correlations can be performed using the appropriate PIV software to statistically determine the movement of groups of particles entrained in the flow. The velocity field can be calculated by dividing the displacement of particles between the two images by the time between images.

Alumina ( $\text{Al}_2\text{O}_3$ ) particles with an average diameter of 1  $\mu\text{m}$  (Noah Technologies) are seeded into the premixed fuel and air stream. A small sample cylinder is filled prior to testing and the air flow through the cylinder, combined with light agitation, is sufficient to loft enough particles into stream. The particles are assumed to be small enough to adequately follow the flow of the fluid in the region of interest. Previous tests have shown that, at high seeding densities, the existence of non-reacting particles through the flame will cause a change in reactivity, likely due to radiative heat losses. An assumption is made that the current seeding densities are comparatively low, and thus do not affect the flame position within the region of interest.

Fig. 3–2 describes the optical configuration of PIV experiment. The laser sheet is generated from the double-pulsed emission of a Nd:YAG (Spectra-Physics) at a

frequency doubled wavelength of 532 nm. The laser beam is manipulated by a series of prisms and lenses made of BK7 borosilicate glass. The light is bent by a series of prisms and directed towards the interrogation area. The light is expanded using a two-lens telescope (concave and plano-convex spherical lenses) and formed into a sheet less than 1 mm thick by a cylindrical prism. The top and bottom edges of the light sheet were then chopped using an iris diaphragm. When the light sheet intersects the flow, it is scattered by the seeded alumina particles and is detected by a Cooke pco.2000 CCD camera equipped with a 90 mm Tamron  $f/2.8$  camera lens. The CCD camera is linked with a Stanford Systems DG535 timing delay generator, thus allowing for a synchronization between pulse emission and camera exposure. Please refer to [22], which contains precise details of PIV timing delays and laser settings. A 1 nm wide bandpass filter, centred around the emitted laser wavelength, is used to reduce the noise and light intensity from the flame region while allowing the scattered laser light through to be detected by the CCD.

### **3.1.5 Nitric oxide concentration measurements - Planar Laser-induced Fluorescence**

Fluorescence of nitric oxide molecules is achieved by exciting along the DiRosa transition at 226.034 nm using a Sirah Cobra Dye Laser, pumped by the Nd:YAG laser at 355 nm. The dye laser, when pumped by YAG, absorbs the incoming beam and re-emits it at a specified wavelength, allowing for precise control over the LIF excitation wavelength. The dye laser is equipped with a double dye cell configuration consisting of a oscillator/pre-amplifier cell and a larger amplifier cell. The 355 nm pumping pulse enters the dye laser and is directed into each of these cells by an

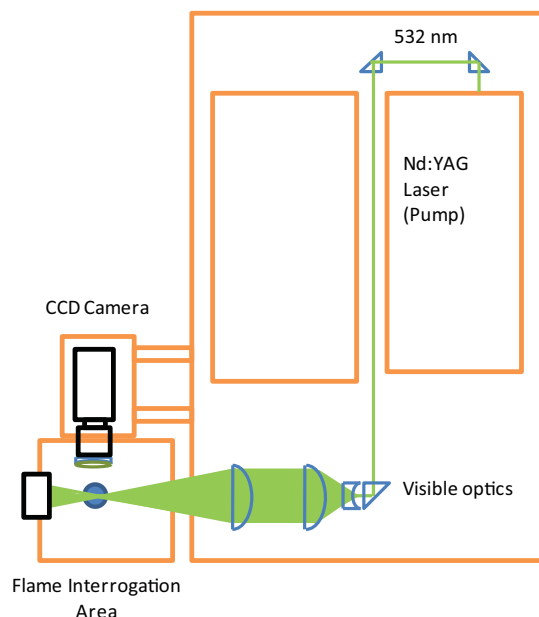


Figure 3–2: Particle image velocimetry (PIV) experimental optics configuration.

array of optics. The cells contain a mixture of Coumarin 450 dye (7-(ethylamino)-4,6-dimethyl-2H,-1-benzopyran-2-one) and pure ethanol solvent, which are circulated to and from a larger reservoir by dye pumps. The oscillator/pre-amp cell contains dye at a concentration of 0.2 g/L with a total reservoir volume of approximately 500 mL. The amplifier cell/reservoir system contains dye at a concentration of 0.0667 g/L and a total volume of approximately 1 L. Coumarin 450 dye was selected because it provided peak fluorescence efficiency at 450 nm which is very close to the desired excitation wavelength when it is frequency doubled to 225 nm. The wavelength exiting the dye laser can be controlled using Sirah Dye software, which changes the angle of a diffraction grating within the laser and thus the output wavelength. The output wavelength can also be halved by the activation of a mounted barium borate (BBO) frequency-doubling crystal. With the BBO crystal enabled, the wavelength

exiting the dye laser is actually half of the defined wavelength in the laser software - for example, a setting of 452.00 nm in the dye laser software corresponds to an output wavelength of 226.00 nm.

All the optics within the dye laser, as well as calibration of the doubling crystal, were aligned for optimal performance by a technician from Newport Corp. The pulse length of the dye laser is 9 ns and the frequency of emission is 10 Hz.

The exact excitation wavelength could not be measured due to lack of appropriate equipment. The  $P_1(23.5)$ ,  $Q_1+P_{21}(14.5)$ ,  $Q_2+R_{12}(20.5)$  transition was selected for excitation at a wavelength of 226.034 nm. Selection of NO excitation wavelength was based on literature and simulation - from LIFsim [10] at an estimated flame temperature of 1500 K, there are excitation peaks at 226.03 nm, 226.058 nm, and 226.07 nm (Fig. 3-3). Although the dye laser may be set to a certain wavelength, the actual emitted wavelength cannot be confirmed. This uncertainty is reduced by performing an excitation scan prior to measurement as described in Section 3.2.3.

### 3.1.6 UV Optics and Signal Collection

The UV pulse is turned several times by 90° right angle prisms before it is sent into a two lens telescope consisting of a concave spherical lens ( $f = -50.0$  mm,  $D = 25$  mm) and a convex spherical lens ( $f = 300$  mm,  $D = 50$  mm). The expanded beam is formed into a vertical sheet using a cylindrical lens ( $f = 400$  mm,  $x = y = 50.8$  mm) and the edges are clipped by an iris diaphragm. The optics are aligned such that the beam waist would be at a minimum over the interrogation area between the nozzle and stagnation plate. The light sheet is estimated to be  $\sim 0.5$  mm in width and  $\sim 15$  mm in height. All optics were obtained from CVI Melles Griot and are made of

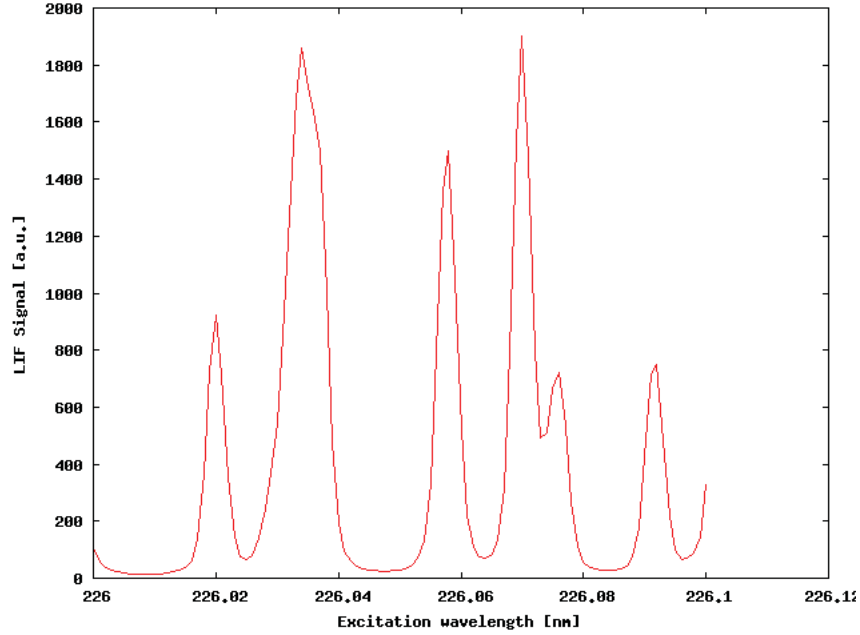


Figure 3–3: Simulated excitation scan of NO-LIF around 226 nm by LIFsim.

uncoated fused silica, which passes light at a broad range of wavelengths. The UV beam steering assembly and signal collection apparatus can be seen in Fig. 3–4.

The total power of the UV sheet per pulse is measured by a Newport pyroelectric energy detector head (818E-05-25-S) with a Newport 1918-C power meter.

Fluorescence of NO molecules is collected by a convex spherical lens ( $f = 150$  mm,  $D = 25$  mm) perpendicular to the beam sheet and focused onto the imaging slit of a 300 mm Acton SP2300 Imaging Spectrometer (Princeton Instruments). The position of the spectrometer is bolted to the table and held in place by a vertical translation stage (Thorlabs). The spectrometer is controlled by Acton Monochromator software, allowing for the rotation and movement of various gratings installed within the spectrometer. The gratings diffract the incoming light and separate the

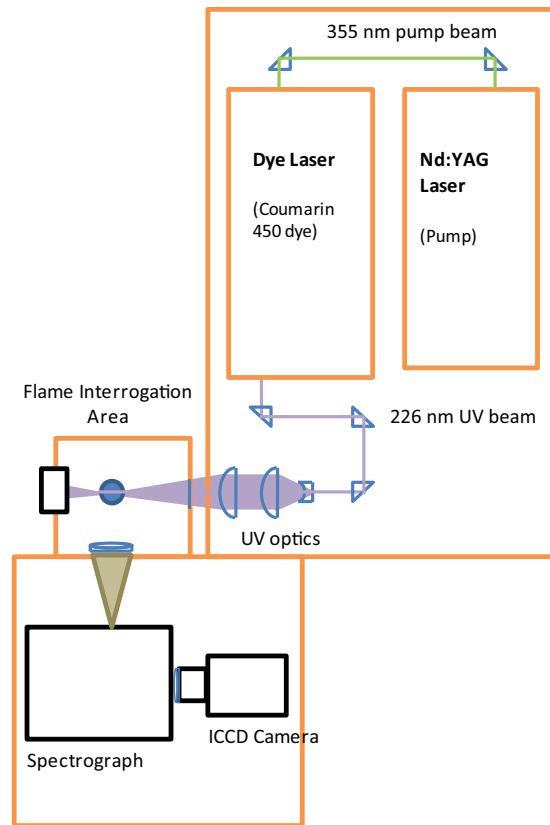


Figure 3–4: The UV optics arrangement and PLIF signal collection set-up.

incoming signal into different wavelengths along the horizontal axis of the grating. Thus, monochromatic light would appear as a single, vertical line at the specified wavelength, while pure white light would appear as a uniform range of signals spread across the visible spectrum. The spectrometer can be focused on a desired wavelength, effectively acting as a bandpass filter, eliminating all signals outside of the wavelength detection window. The installed grating is blazed H-UV and has 1200 grooves/mm.

A UV-intensified CCD camera (Cooke DiCam Pro) is used to capture the NO fluorescence spectrum and output to a desktop computer for analysis. The ICCD camera is utilized at a gain level of 99%, thus allowing significant amplification of the fluorescence signals for processing. The camera trigger is linked to a Stanford Systems DG535 timing delay generator such that the camera exposure is synchronized with the pumping laser pulse. The pump laser Q-switch is triggered 170  $\mu$ s after the lamps are fired. The camera is set to capture a 200 ns exposure exactly 171000 ns after the lamps are fired within the Nd:YAG pump laser - the delay time and exposure time were found empirically to provide good fluorescence signals while limiting background noise. The ideal timing settings for the camera/laser trigger were determined through trial and error.

The size of the CCD detector is 1280 x 1024 pixels. A vertical and horizontal binning mode of 8 was used, thus summing 8 x 8 pixels together to create a stronger signal intensity per pixel. The resulting image size is 160 x 128 pixels.

Due to the steady nature of the stagnation flame geometry, it is possible to average over a set of multiple images, thus reducing the overall uncertainty in the measurement.

### **3.2 Experimental Procedure - Obtaining Measurements**

This section attempts to detail the experimental procedure followed to obtain raw NO-PLIF measurements. In general, measurements were performed in a team of two experimenters - one person operated the flow control system and dye laser system while the other controlled the camera recording and maintained laser power.

### 3.2.1 Heating and flow temperature

Prior to any experiments, all elements are heated to 85°C using the heating system detailed in the above sections. Air is flowed through the system at a chosen experimental flow rate and a flow probe (Type-K thermocouple mounted on a traversing stand) is inserted to measure the temperature of air exiting the nozzle. The flow temperature, while not measured during each run, was monitored with the probe between runs.

### 3.2.2 Laser power measurements

When the system is nearing equilibrium temperatures around the setpoint, the Nd:YAG-Dye set-up is warmed up to the desired laser power. The UV laser system was found to require about 20 minutes of runtime to achieve a relatively stable power output. The power of the light sheet is measured by the powermeter after the sheet has left the collection volume. When the powermeter was placed in this position for optimal power measurement, large amounts of laser light is scattered into the collection optics - the powermeter must be replaced with a beam dump during data collection. The power of the laser was measured before and after each experimental run to ensure a constant power output. It should be noted that the power measurement yielded large fluctuations of power at times - it was not clear whether these fluctuations were physical or resulted from bad equipment readings. The average value over several minutes was taken to be the true measurement of laser power.

All measurements were taken at a laser sheet energy of  $\sim 0.5$  mJ. This excitation power was selected because it is well within the linear excitation regime of the NO

molecules and is low enough to be economical with dye degradation. It was found that at high powers, the laser dye degrades quickly and will need to be frequently changed. Refer to Appendix B for information regarding dye maintenance and Appendix F for recommendations on preparing the dye.

### **3.2.3 Excitation scan and wavelength check**

Before any data is taken, an excitation scan was performed with the dye laser to account for wavelength drift in the laser. Due to the inability to directly measure the output wavelength of the UV beam, this was a necessity to keep the exciting wavelength constant between all fuels. An unseeded stagnation flame was lit and the scan was performed by the dye laser for wavelengths between 452 nm and 452.1 nm (resulting in a frequency-doubled wavelength between 226.0 nm and 226.05 nm). The wavelength of highest excitation was selected and the current dye wavelength setting was assumed to be equal to the theoretical peak excitation of 226.034 nm corresponding to the DiRosa transition. In all fuel cases, it was found that the measured peak of fluorescence corresponded fairly closely to the theoretical transition - a dye laser setting of approximately 452.04 nm, which yields a 226.02 nm UV beam when doubled.

An off-line excitation scan was also performed to determine an appropriate wavelength for background measurements to be used in the signal processing stage. The scan was performed in the general vicinity of the on-line wavelength and a wavelength was selected which would yield the minimum amount of fluorescence signal. It was found that a dye laser setting of approximately 452.07 nm, yielding 226.035 nm corresponded to the lowest fluorescence signal, and thereby best background signal.

Fig. 3-5 is a simulated excitation profile between 226.0 nm and 226.1 nm with lines describing both the theoretical peak transition and background location.

A difference of  $\sim 0.013$ - $0.014$  nm between theoretical (226.034 nm) and measured (226.020 nm) excitation peaks was similar to the difference between theoretical (226.048 nm) and measured (226.035 nm) excitation minima, indicating a systematic wavelength drift in the dye laser. This was accounted for by performing an on-line and off-line excitation scan every day prior to taking experimental measurements.

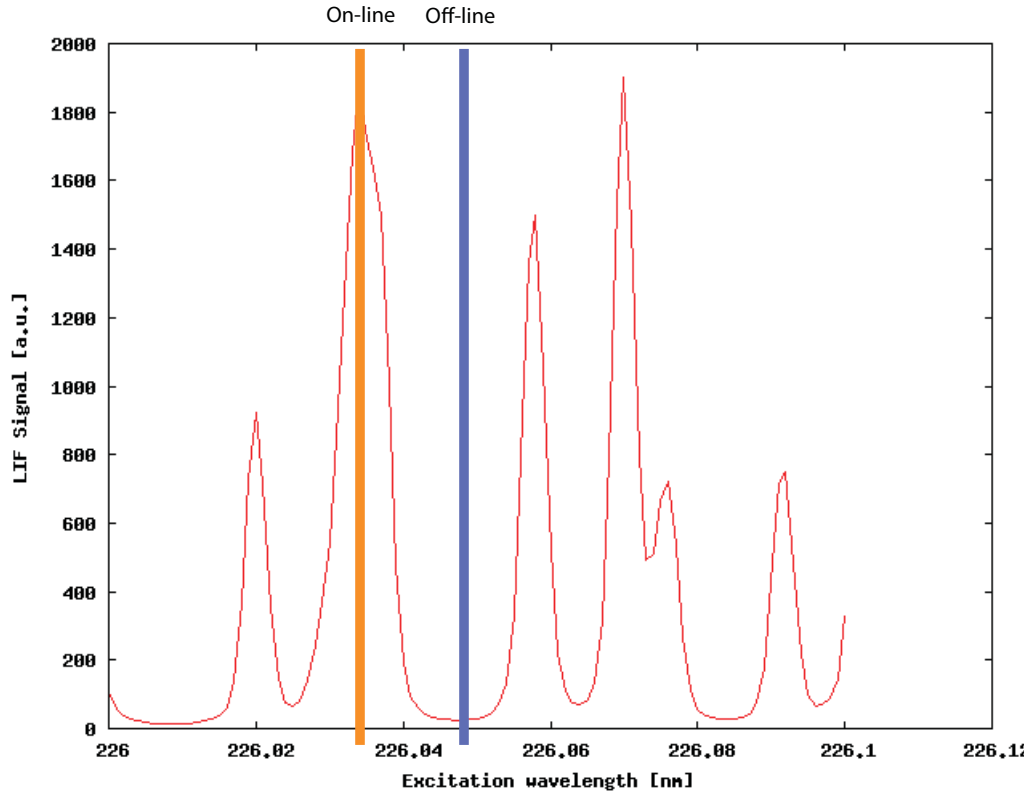


Figure 3-5: Simulated excitation scan marked with 226.035 nm peak transition (on-line) and 226.048 nm minimum (off-line).

### 3.2.4 Stagnation Flames

The experimental set-up of the stagnation flame burner has been described in detail in Section 3.1.1. Stagnation flames were lit using a barbecue lighter and protected from atmosphere using a co-flow of nitrogen gas. The flame was stabilized approximately halfway between the nozzle and stagnation plate. Due to the wide range of flame speeds over the course of an experimental run, it was difficult to maintain a constant flame position. During PIV measurements, flames of different  $\phi$  for the same fuel were kept at a constant flame position, allowing for a direct comparison between the flame speeds under a changing  $\phi$ . However, the flame position was allowed to vary between fuels to the most convenient location of stability. Prior to concentration measurements, it was ensured that the flame was flat and stable in position. Maintaining constant flame position between  $\phi$  was more important for flame speed comparisons, but less so for NO concentration measurements. It was assumed that NO production occurs independently of flow velocity and strain. Thus, should the flames differ in position, a simple shift of predicted NO concentration profiles can be performed to line them up for comparison.

The flow of premixed fuel-air streams was bypassed around the PIV seeding chamber using valves seen in Fig. 3-1. It was found that alumina particles used for PIV often remained in the flow lines and were lofted during PLIF measurements. This led to significant amounts of Mie scattering through the collection volume and diffuse beam scattering as the particles settled on the stagnation plate. Due to the difficulties in cleaning the system of alumina particles, all PLIF measurements were

generally performed and completed first before taking PIV measurements. Please refer to Appendix B for details regarding maintenance of the flow system.

### 3.2.5 PIV Measurement Method

Particle image velocimetry was performed using the equipment and settings detailed in the Section 3.1.4. A series of 314 image pairs were captured using the Cooke CCD camera and saved for processing. Prior to image capture, the flame was lit and stabilized at the desired flame location. Particles were lofted into the flow by agitation of the particle seeding chamber – the appropriate particle concentration was determined subjectively by the operator of the camera system.

PIV was performed for all fuels at  $\phi = 0.8, 1.0$  and  $1.3$ .

The image pairs for each run were processed using DaVis PIV software from LaVision. The imaged flow field is translated into a field of velocity vectors defined by the flow of alumina particles. A sum-of-correlation routine was used with round pixel windows reducing from  $64 \times 64$  pixels to  $32 \times 32$  over 3 loops. Lanczos reconstruction was also applied to all images for post-processing.

The centreline velocity of the flow, assumed to be one-dimensional in the axial direction, is taken and plotted in MATLAB. Fig. 3–6 shows the axial velocity plot beside a photo of a stagnation flame for comparison. Experimentally determined values such as radial velocity gradient, flow speed and location are then used as a basis for stagnation flame simulations in Chemkin [18]. Additional information regarding the PIV method can be found in [22, 50].

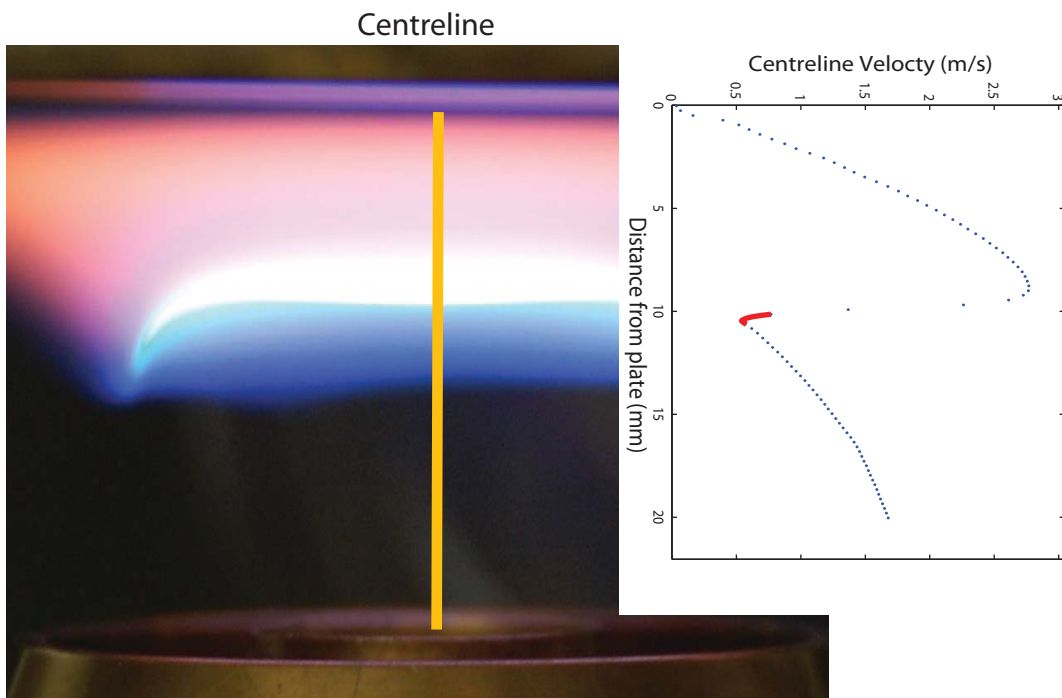


Figure 3-6: A *n*-butanol flame,  $\phi = 1.0$ , seen with the corresponding centreline axial velocity plot.

### 3.2.6 NO-PLIF Measurement Methodology

PLIF measurements were taken using the equipment and settings detailed in the Section 3.1.5. Appendix A describes the steps taken to obtain accurate spatial measurements in the collection apparatus.

The investigation of NO production between fuel types was carried out by obtaining PLIF measurements for the four fuels – *n*-butanol, *iso*-butanol, *n*-butane and *iso*-butane – burned at the three equivalence ratios  $\phi = 0.8, 1.0$  and  $1.3$ . As a comparison of NO production between similar alkane and alcohol fuels, *n*- and *iso*-butanol was matched with *n*- and *iso*-butane. For each fuel case, the runs were performed as described in Table 3–1.

All experimental runs were performed with a measured laser power of  $\sim 0.5$  mJ. 500 images were recorded for each run for both on-line and off-line signal measurements. The off-line measurements were taken for background subtraction purposes. Recording a large number of images greatly reduces the overall random error contained within the mean of all images.

The Camware software was used to record images from the ICCD camera during experiments. The native file type of Camware is \*.b16, which is a PCO graphic file

Run #	Seeding	$\phi=0.8$	$\phi=1.0$	$\phi=1.3$	Purpose
1	•				Beam profile
2	•	•			Quantitative signal calibration
3. a		•			Measurement - $\phi=0.8$ flame
3. b			•		Measurement - $\phi=1.0$ flame
3. c				•	Measurement - $\phi=1.3$ flame

Table 3–1: Runs performed for NO-PLIF measurements for each fuel case

– in order for analysis of the images, a converter was used to modify the file type to 16-bit \*.tiff. The PCO converter was obtained through direct communication with support staff from the Optikon Corporation. With the image conversion, it became possible to read image files into Matlab for processing and analysis.

To process the raw image data in the \*.tiff files, several MATLAB scripts were written to read and average a data series - typically consisting of a sequence of images shot in the same experimental run. The averaging occurs for each pixel location across the entire range of the data series, thus allowing for the creation of a single \*.tiff image which represents the mean measurement of the series (Fig. 3–7, right). The horizontal width of the figure describes the wavelength of the incoming light, separated by the spectrograph. The vertical axes in Fig. 3–7 describe the spatial  $y$ -axis of the measurement, representing the axial location of fluorescence between the nozzle and plate in the stagnation flame geometry. Note that because of the collection lens, the signal is flipped along the horizontal axis. The averaged raw data was then subjected to multiple corrections and correlations described in later sections.

The first band of fluorescence corresponding to the A-X(0,1) NO transition was found to be the strongest PLIF signal when averaged. This fluorescence band, located at  $\sim 236$  nm, was herein used as representative of the total fluorescence signal measured. This is valid since the signal received from this transition will scale according to the total fluorescence signal despite the fluorescence occurring at the other transitions. The processing script was used to average across the width of

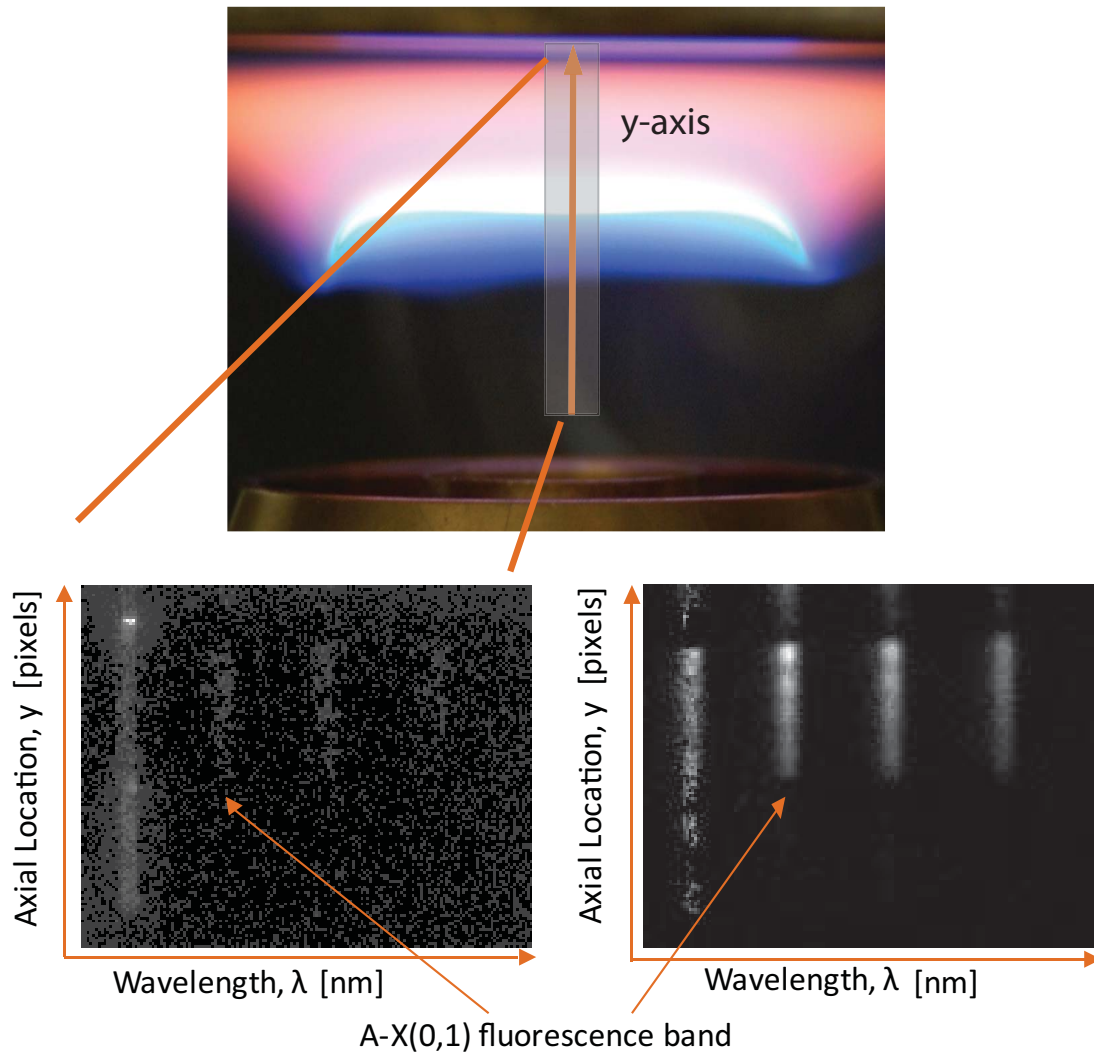


Figure 3-7: Top: Stagnation flame with overlaid spatial  $y$ -axis. Left: A single raw image of NO-PLIF in the shaded zone. The spatial coordinate ( $y$ -axis) is flipped due to the spherical collection lens. Right: NO-PLIF averaged over 500 images after background subtraction.

the fluorescence band to find the mean PLIF signal profile over the measured axial locations.

Once raw signal manipulation for each run was completed, significant amounts of signal post-processing were required to achieve quantitative concentrations from the relative values of the PLIF signals. All post-processing was carried out using routines written in MATLAB. Chapter 4 describes the post-processing conducted in detail.

### **3.3 NO Profile Simulations**

#### **3.3.1 Model and Mechanisms**

Stagnation flame simulations are performed using the stagnation flame model in CHEMKIN-PRO (v15) [18]. The NO production profiles generated with these simulations can then be compared to experimental findings. The resulting evaluation can provide additional validation to the models and aid in the future refinement of the kinetic mechanisms.

NO production from *n*-butanol flames was simulated using the Sarathy-Dagaut butanol mechanism and the GDF\_kin3.0 NO<sub>x</sub> sub-mechanism. The base butanol mechanism, which did not contain NO<sub>x</sub> chemical reactions, was modified by inserting the NO<sub>x</sub> reactions into it from GDF\_kin3.0 and adding the complementary thermodynamic and transport data. The resulting mechanism contains 139 (118 base + 21 NO<sub>x</sub>) species and 1067 (878 + 189) reactions. Refer to Appendix D for details regarding manipulation of chemical kinetic mechanisms.

*n*-Butane flames are simulated with the USC\_Mech Version II mechanism combined with the same NO<sub>x</sub> sub-mechanism. The resulting mechanism contains 132 (111 + 21) species and 973 (784 + 189) reactions.

At the time of writing, there were no mechanisms available to simulate NO<sub>x</sub> formation for *iso*-butanol, thus the simulations were focused on contrasting *n*-butanol and *n*-butane.

### 3.3.2 Initial Conditions

For these two fuels, flames of  $\phi = 0.8, 1$  and  $1.3$  are simulated using the Stagnation Flame model in Chemkin [18]. The stagnation flame burner requires the following inputs for simulation: reactant mole fractions, pre-flame flow temperature, stagnation plane temperature, inlet flow velocity, distance from flow input to stagnation plane and radial velocity gradient. The temperature information was measured using thermocouples in the experiment. The reactant mole fractions of fuel and air were predefined for each case. The remaining flow information was taken from experimental PIV information of the simulated flame. Appendix E contains the values of the boundary conditions used in simulations.

For all cases, the initial domain was given 10 uniform grid points with 100 possible adaptable grid points. The maximum number of grid points was set to 700. The mechanisms with added NO<sub>x</sub> chemistry are generally stiff and require many continuations to aid in convergence. The initial gradient and curve parameters were taken at 1.0 each, with every subsequent continuation reducing both parameters the same amount. These parameters are defined by the change of value between two grid points – for example, if the gradient between two points was larger than the defined

parameter, then more points would be added to ‘smooth’ out the gradient. The final gradient and curve parameters were reduced to 0.1 each. The model was judged to be converged at this point as there were generally 300+ grid points and the solution had not changed more than 1% from the last continuation.

The resulting data from the simulation is imported and processed using the Chemkin Graphical Post-processor [18] – the output is a \*.ckcsv file which can be analyzed or plotted using MS-Excel. A script was written to import the relevant simulation data into MATLAB and plot it against the corresponding experimental data.

## CHAPTER 4

### PLIF Signal Post-processing

#### 4.1 Background Subtraction

Despite attempts to experimentally reduce background noise obtained during signal collection by eliminating stray or scattered light, it was necessary to perform a background subtraction routine to further increase signal-to-noise ratio. A noise level of approximately 100 counts of signal intensity was consistently seen throughout the entire image. It was also found that collection optics contribute towards increased noise at the edges of the image.

To clean up the background noise in all calibration cases, a background subtraction method was used as described in Section 2.3 and by Thomsen et al. [57]. The signals from the raw off-line excitation were averaged at each pixel over the total number of images, forming an average background signal for the run. The average background image was subtracted from the averaged on-line signal image, thus removing the noise from the positive signal.

#### 4.2 Simplifying the Problem

A challenge with processing the resulting signal from experiment occurs with the ability of the detector to measure NO fluorescence spatially. While it is desirable to obtain spatial information when measuring NO species profiles before and after the flame front, several factors will change as a function of spatial location (hereby denoted as the  $y$ -coordinate). Recall from Section 2.2.1, that the planar laser-induced

fluorescence within the collection volume can be written as a function of several constant and spatially varying terms as in Eq. 2.2. Also recall that  $n_i^\circ(y)$  and  $\rho_\nu(y)$  are defined in Eq. 2.3 and Eq. 2.4 respectively.

It is experimentally inefficient to measure each quantity in Eq. 2.2 individually. The experiment and post-processing procedures were designed to reduce Eq. 2.2 into measurable quantities. The eventual goal would be to simplify the equation into a simple linear relationship between the measured PLIF signal,  $P_d(y)$ , and the ground state population of NO,  $n_i^\circ(y)$ :

$$P_d(y) = Cn_i^\circ(y)$$

where  $C$  is a constant.

### 4.3 Normalization by Laser Sheet Intensity - Run 1

The purpose of Run 1 is to remove the variation of laser sheet intensity and optical collection from Eq. 2.2.

The beam profile of the laser upon exit from the dye laser was found to be extremely non-uniform. These non-uniformities in intensity are further exacerbated by the expansion and manipulation of the beam by the UV optics prior to interrogation. While not ideal, it is possible to still perform spatial measurements of NO concentration because it is known that fluorescence signal is linearly scaled with excitation power. Additionally, the solid angle  $\Omega_c(y)$  changes with respect to the  $y$ -coordinate and represents the various  $y$ -dependent aberrations and distortions in the collection optics.

In Run 1, a known concentration of NO molecules was introduced into a flow of O<sub>2</sub>/N<sub>2</sub> mixture and the resulting fluorescence of the cold flow was measured. Given a completely uniform excitation sheet and non-distorting collection optics, this constant concentration seeding of NO would normally result in a constant PLIF signal. However, due to systematic non-uniformities, this was found to not be the case experimentally. Because there is constant seeding and temperature, the spatial fluctuations in the fluorescence signal are caused by these systemic non-uniformities in the laser sheet and collection optics.

Referring back to Eq. 2.2, it can be assumed that the effects of all terms not related to the laser sheet or optics can be lumped into a single term,  $D$  for each location along the  $y$ -coordinate. Due to the constant seeding concentration and flow temperature,  $n_i^\circ(y)$  is a constant term and may be lumped with  $D$ . Recall that  $f(y)$  represents a normalized function describing spatial fluctuation in laser sheet intensity. Also note that  $I_{\text{laser,total}}$  is kept constant for all experimental runs and can be lumped with  $D$ .

$$P_{\text{beam}}(y) = D\Omega_c(y)f(y) \quad (4.1)$$

$$D = h\nu_{\text{ul}} \left( \frac{A_{\text{ul}}B_{\text{ul}}}{Q_{\text{ul}}} \right) \frac{1}{4\pi} V_c n_{i,\text{beam}}^\circ I_{\text{laser,total}} \quad (4.2)$$

Therefore, the measurement of  $P_{\text{beam}}(y)$ , the Run 1 PLIF signal, will give the product of  $\Omega_c(y)$  and  $f(y)$ . The signal is then normalized to create a beam intensity distribution function:

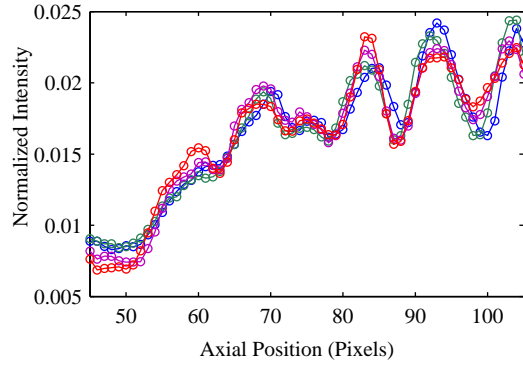


Figure 4–1: Normalized beam distribution functions for all fuels measured with a constant seeding of 45 ppm.

$$\frac{P_{\text{beam}}(y)}{\int P_{\text{beam}}(y)} = \frac{D\Omega_c(y)f(y)}{\int P_{\text{beam}}(y)}$$

$$\hat{P}_{\text{beam}}(y) = D'\Omega_c(y)f(y)$$

Fig. 4–1 displays the normalized beam distribution functions,  $\hat{P}_{\text{beam}}(y)$ , for all four fuels taken over the course of several days. The figure not only illustrates the non-uniformity in the laser intensity distribution and collection optics, but also describes the day-to-day variation in beam profile. It is thus essential to perform a beam profile measurement frequently.

Given the assumption that  $\Omega_c(y)$  and  $f(y)$  do not change over the course of a day, the normalized beam function  $\hat{P}_{\text{beam}}(y)$  can be used to eliminate them for all subsequent measurements. The measured signals of subsequent runs are divided by the beam profile, thus making the resulting signal independent of laser sheet intensity and aberrations in the collection optics:

$$\frac{P_{\text{measured}}(y)}{\hat{P}_{\text{beam}}(y)} = \left(\frac{1}{D'}\right) h\nu_{\text{ul}} \left(\frac{A_{\text{ul}}B_{\text{ul}}}{Q_{\text{ul}}}\right) \frac{V_{\text{c}}}{4\pi} n_i^{\circ}(y) I_{\text{laser, total}}$$

By lumping together all the constant terms into  $D''$ , the remaining equation becomes:

$$\frac{P_{\text{measured}}(y)}{\hat{P}_{\text{beam}}(y)} = (D'') \left(\frac{Q_{\text{ul, beam}}}{Q_{\text{ul, measured}}}\right) n_i^{\circ}(y) \quad (4.3)$$

where  $n_i^{\circ}(y)$  is previously defined in Eq. 2.3 as the product of  $\chi_{[\text{NO}]}(y)$  and  $\frac{N}{V}(y)$ . Also note that  $Q_{\text{ul, beam}}$  has been taken from  $D'$  and not lumped with  $D''$  – it is better to consider the quenching terms together for future discussion.

$$\bar{P}_{\text{measured}}(y) = (D'') \left(\frac{Q_{\text{ul, beam}}}{Q_{\text{ul, measured}}}\right) n_i^{\circ}(y) \quad (4.4)$$

$\bar{P}_{\text{measured}}(y)$  represents a measured fluorescence signal which has been normalized by the beam profile.

$\bar{P}_{\text{measured}}(y)$  is equal to the product of  $n_i^{\circ}(y)$ , quenching terms and the constant  $D''$ . While the normalization has greatly simplified the equation, it is difficult to solve for these unknowns either analytically or experimentally, necessitating the need for further corrections or calibrations.

#### 4.4 Calibration Technique through constant NO seeding - Run 2

In Run 2, the NO seeding calibration technique was used to infer the values for the constants and unknowns in Eq. 4.4 through precise control of the NO concentrations introduced into the flame. The goal of this technique is to obtain relative signal intensities corresponding to different seeded concentrations allowing for the

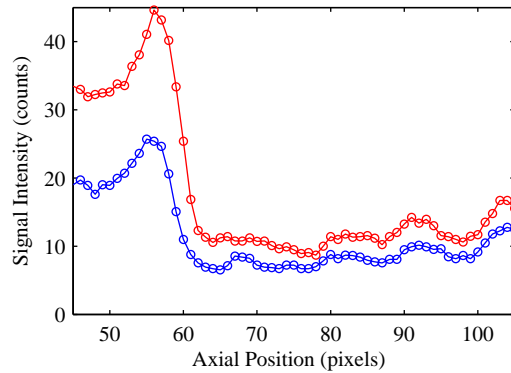


Figure 4-2: Raw calibration signals: *n*-butanol flame  $\phi=0.8$  seeded with 28 ppm (blue) and 45 ppm NO (red).

generation of a calibration curve. The calibration can then be used to quantitatively determine the NO concentration of any flame by measuring fluorescence signal.

Like Run 1, the flow is seeded with a known concentration of NO molecules. The calibration technique, however, involves using a lean flame as a calibration flame, which simulates a post-flame condition that is similar to all other measured flames. In all fuel cases, a lean flame ( $\phi=0.8$ ) is lit in a premixed flow with 21% O<sub>2</sub> gas by volume. The different seeding concentrations are created by mixing a stream from a gas cylinder of 150 ppm NO/N<sub>2</sub> with different mixtures of O<sub>2</sub>/N<sub>2</sub>. The flows were mixed proportionately to yield a final mixture that, like air, contains 21% O<sub>2</sub> by volume. A table of flow rates and gas mixtures used in calibration can be found in Appendix C. Fig. 4-2 shows the two raw calibration flame signals, which have undergone background subtraction but have not yet been corrected for non-uniformities in beam sheet intensity.

A key assumption of the application of this technique is that  $Q_{ul,beam} \approx Q_{ul,measured}$  between flames at different equivalence ratios for the same fuel. It is known, however, that  $Q_{ul}$  varies with temperature and species concentration in the post-flame region. Corrections associated with the difference in  $Q_{ul}$  between  $\phi = 0.8$  calibration flames and  $\phi = 1.0$  and  $1.3$  flames will be required for increased accuracy of measurements. These corrections involve scaling the simulated difference in  $\bar{P}_{measured}(y)$  between flames and applying a correction factor to the stoichiometric and rich cases.

A lean,  $\phi = 0.8$  flame was chosen because it can be assumed that there is negligible consumption of seeded NO molecules through the flame and that the seeded NO concentration is low enough not to affect further NO production. These assumptions are supported by several re-burn experiments [3, 57] as written in Section 2.3.

Once again, obtaining calibration measurements for the post-flame region is essential for eventually relating a non-seeded NO measurement to a quantitative concentration. Recalling that the ground state population of NO is the product of mole fraction and number density (Eq. 2.3), the post-flame region will significantly reduce the number density due to expansion of burned gases. Fig. 4-3 shows that this effect can be captured spatially through calibration measurements once the beam profile non-uniformity is removed by dividing by the normalized beam distribution function measured in Run 1. By seeding the flow with a given concentration of NO, the variations in flame temperature will be accounted for by a corresponding change in NO concentration post-flame.

The calibration flame will itself produce a native amount of NO molecules leading to a variation in mole fraction  $\chi_{[NO]}(y)$  with respect to  $y$ . The NO produced by the

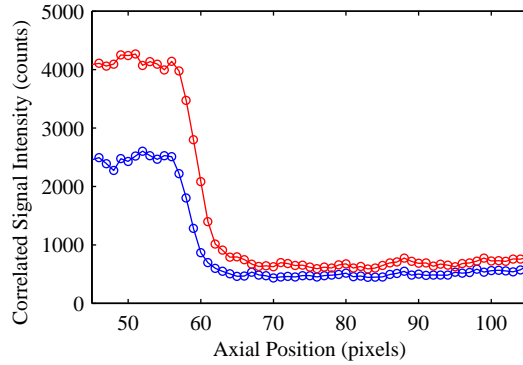


Figure 4-3: Correlated calibration signals with beam non-uniformity removed: *n*-butanol  $\phi=0.8$  flame seeded with 28 ppm (blue) and 45 ppm NO (red).

flame cannot be experimentally distinguished from those seeded into the flow. It is important to separate the relative signal generated by seeded NO from the flame-produced NO in order to create an accurate calibration curve. Under the assumption that the seeded NO molecules do not significantly alter further production of NO through the flame, the total PLIF signal is simply the sum of individual signals. Thus, if the NO signal profile of the unseeded lean flame is subtracted from the calibration signal profile, the remainder will be the NO signal attributed to the seeded NO amount.

$$P_{\text{calibration}}(y) = \bar{P}_{\text{measured}}(y)$$

$$P_{\text{calibration}}(y) = P_{\text{seeded}}(y) + P_{\text{native,lean}}(y)$$

$$P_{\text{seeded}}(y) = P_{\text{calibration}}(y) - P_{\text{native,lean}}(y)$$

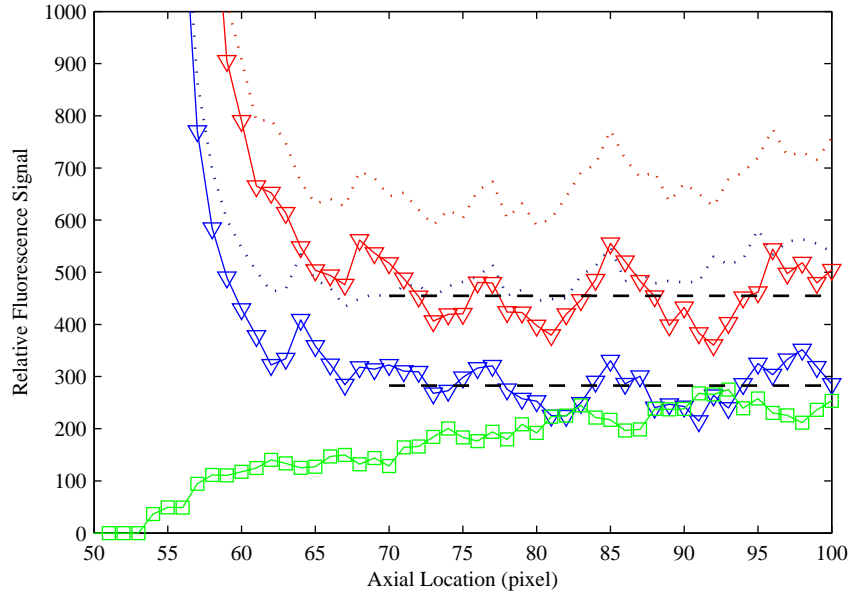


Figure 4-4: *n*-butanol calibration flame  $\phi = 0.8$ , seeded with 28 ppm (blue) and 45 ppm (red). Uncorrected (dot), corrected ( $\nabla$ ) with averaged post-flame values (dash). Lean  $\phi = 0.8$  native NO ( $\square$ ).

Fig. 4-4 shows the large change between corrected and uncorrected seeding signals. The corrected measurements were shown to yield much better calibration results.

With knowledge of the NO ground state population,  $n_i^\circ(y)$ , by seeding a defined NO concentration, and dividing through by the normalized beam profile  $\hat{P}_{\text{beam}}(y)$ , there are only two remaining terms in Eq. 4.4. The quenching terms,  $Q_{\text{ul}}$  are temperature and species dependant and thus will take different values for the pre- and post-flame regions. Looking exclusively at the post-flame region:

$$P_{\text{seeded}}(y) = (D'') \left( \frac{Q_{\text{ul,beam}}}{Q_{\text{ul,calibration}}} \right) n_{i,\text{seeded}}^\circ(y)$$

$$P_{\text{seeded}}(y) = C_{\text{calib}} n_{i,\text{seeded}}^{\circ}(y) \quad (4.5)$$

where  $C_{\text{calib}}$  is a constant determined through measurement of the seeded NO in the calibration flame. Therefore, a linear equation has been defined for which a known seeded amount of NO,  $n_i^{\circ}(y)$ , will yield a measured corrected calibration signal,  $P_{\text{seeded}}(y)$ . A calibration line can be defined from Eq. 4.5 using NO concentration on the x-axis and corrected calibration signal.

$$y = C_{\text{calib}}x$$

As seen in Fig. 4–4, each seeding case has an average taken for the post-flame corrected calibration signal - this average then is used as the value at which the relative fluorescence signal corresponds to the known concentration of NO seeding. A calibration curve is created by fitting a line using each seeded concentration as a point on the curve. To improve the fit, an additional point at the origin (0,0), representing zero signal given zero concentration, was added to the data set.

Figure 4–5 shows a calibration curve using averaged corrected data from Fig. 4–4. Using the slope of the calibration curve, any PLIF signal obtained for the same experimental set can be referenced to a NO concentration. In Section 4.5, the curves will be used to achieve quantitative spatial measurements of NO concentration in unseeded flames.

Calibration curves have been found to be portable between equivalence ratios under the same pressure conditions and dilution, due to similar off-line background signals [57]. Thus, a single calibration curve for each fuel was created using the

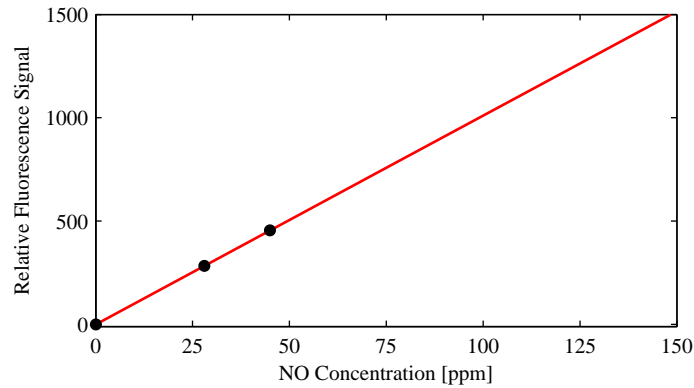


Figure 4–5: Calibration curve generated using averaged post-flame corrected signal: *n*-butanol  $\phi=0.8$  calibration flame seeded with 28 ppm and 45 ppm.

calibration flame and was then used for other equivalence ratios. Four calibration curves were used in total, one for each fuel.

#### 4.5 Measurement of Unseeded Flames - Run 3

Following Run 1 and Run 2, three unseeded flames ( $\phi = 0.8, 1.0$  and  $1.3$ ) for each fuel were stabilized in the apparatus and NO-PLIF measurements were taken. The flows consisted of premixed fuel and air, heated to a temperature of approximately  $85^{\circ}\text{C}$ . The flames were kept at a relatively constant location between the nozzle and the stagnation plate by changing the exit flow velocity. In each case, an on-line and off-line measurement was taken using wavelengths determined from the excitation scan performed at the beginning of the experiment. Between each equivalence ratio, the power from the laser was measured to ensure a laser sheet intensity of  $\sim 0.5$  mJ.

Background subtraction was performed on the unseeded NO profiles for each case by subtracting the averaged off-line images from the corresponding averaged on-line images.

After the noise was subtracted, quenching corrections were made to each of the unseeded profiles. Quenching has previously been described as a non-radiative collision of an excited molecule with another molecule.  $Q_{ul}$  is temperature dependent and also dependent on the different collisional cross-sections of product species - the post flame region contains different mole fractions of products for the different equivalence ratios. Quenching coefficients for the major product species within flames ( $N_2$ ,  $O_2$ ,  $CO$ ,  $CO_2$ ,  $CH_4$ ,  $Ar$ ) have been measured in past studies. LIFsim includes the quenching coefficient measurements in its database [54] and can simulate the relative fluorescence signal of NO under different quenching conditions and temperatures. The relevant equilibrium species mole fractions and temperature were input into LIFsim, producing an emission spectrum containing the relative signal intensities of the fluorescence bands. Emission spectra were simulated for  $\phi = 0.8$ , 1.0 and 1.3 - the peak signal intensity for the 1st fluorescence band ( $\sim 236$  nm) was taken and compared between the simulations. The correction was created by taking the ratio of signals between the calibration case ( $P_{calib}$ ) and the stoichiometric ( $P_{\phi=1.0}$ ) or rich ( $P_{\phi=1.3}$ ) case. At  $\phi = 1.0$ , the relative detected signal from fluorescence of the same concentration of NO ( $1.12E-16$  in arbitrary units) was found to be much less than that detected at lean conditions ( $1.44E-16$ ).  $C_{calib}$ , the calibration coefficient determined at  $\phi = 0.8$ , is specific to those conditions and will not correspond to  $\phi = 1.0$  or 1.3 conditions without appropriate corrections.

The method of applying corrections is to scale the  $C_{\phi=1.0}$  and  $C_{\phi=1.3}$  to equal  $C_{calib}$  allowing a more accurate application of the calibration curve to quantify NO signals. Temperature and product species mole fractions were calculated at chemical

equilibrium using the Equilibrium model in Chemkin [18]. For simplification, the equilibrium temperatures and species for *n*-butanol and *n*-butane were also used for *iso*-butanol and *iso*-butane respectively. The mechanisms used for the Chemkin calculation were Sarathy-Dagaut for the butanols and USC\_Mech V.II for the butanes.

The following equations detail the derivation of the correction factor,  $C_{\text{corr}}$  for the stoichiometric case.

$$\begin{aligned} C_{\text{corr}} &= \frac{P_{\text{calib}}}{P_{\phi=1.0}} \\ C_{\text{calib}} &= C_{\text{calib},\phi=1.0} (C_{\text{corr}}) \\ C_{\text{calib},\phi=1.0} &= \frac{C_{\text{calib}}}{C_{\text{corr}}} \end{aligned}$$

If the Eq.4.4 is re-written for the case of  $\phi = 1.0$  and Eq.4.5 is used, the resulting equation in terms of  $C_{\text{calib}}$  is:

$$\begin{aligned} \bar{P}_{\text{measured},\phi=1.0}(y) &= \left( D'' \frac{Q_{\text{ul,beam}}}{Q_{\text{ul,calibration}}} \frac{N}{V} \right)_{\phi=1.0} \chi_{[NO]}(y) \\ \bar{P}_{\text{measured},\phi=1.0}(y) &= (C_{\text{calib},\phi=1.0}) \chi_{[NO]}(y) \\ \bar{P}_{\text{measured},\phi=1.0}(y) &= \frac{C_{\text{calib}}}{C_{\text{corr}}} \chi_{[NO]}(y) \end{aligned}$$

$$(\bar{P}_{\text{measured},\phi=1.0}(y)) C_{\text{corr}} = C_{\text{calib}} \chi_{[NO]}(y) \quad (4.6)$$

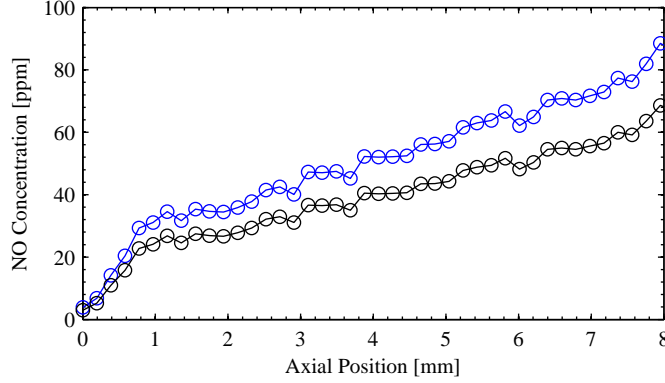


Figure 4–6: Comparison of NO concentration profiles for  $\phi=1.0$  *n*-butanol ( $\circ$ ) with quenching corrections (blue) and without quenching corrections (black)

Eq. 4.6 shows that if the correction factor,  $C_{\text{corr}}$  is applied to the measured and normalized  $\phi = 1.0$  fluorescence signal,  $\bar{P}_{\text{measured},\phi=1.0}$ , it may be used with the calibration curve created by a lean calibration flame. NO signals from  $\phi = 1.3$  flames can be corrected in the same way if the corresponding correction factor is found by taking the ratio  $\frac{P_{\text{calib}}}{P_{\phi=1.3}}$ . No quenching correction was necessary for  $\phi = 0.8$  flames because the calibration was performed under the same conditions. It was calculated that the *n*-butanol  $C_{\text{corr},\phi=1.0} = 1.29$  and for  $C_{\text{corr},\phi=1.3} = 1.05$ . It was calculated that the *n*-butane  $C_{\text{corr},\phi=1.0} = 1.29$  and for  $C_{\text{corr},\phi=1.3} = 1.12$ . The effect of quenching corrections on the final concentration profile can be seen in Fig. 4–6. Please refer to Appendix F for more details on quenching corrections.

#### 4.6 Applying the calibration

After the NO-PLIF signals from flames of  $\phi = 0.8, 1.0$  and  $1.3$  were normalized and corrected for quenching, the signals were interpolated onto the calibration curve developed for the fuel. The interpolation was applied for every spatial point along

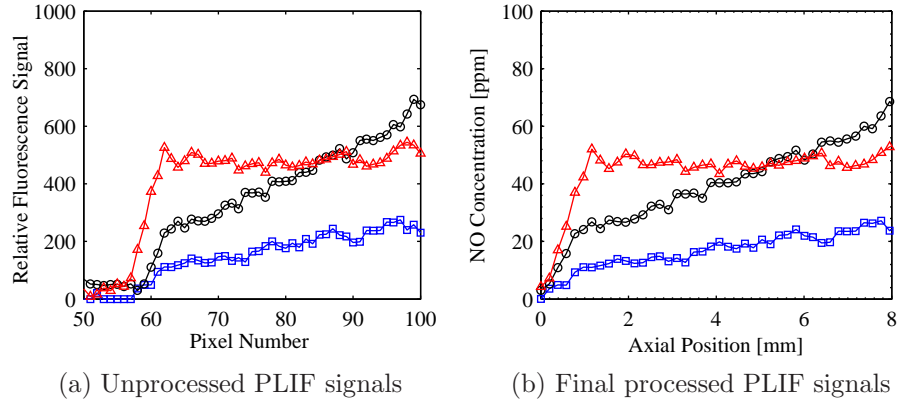


Figure 4-7: NO-PLIF signals from unseeded *n*-butanol flames  $\phi = 0.8$  ( $\square$ ),  $1.0$  ( $\circ$ ),  $1.3$  ( $\triangle$ )

the measurement to attain a NO concentration profile for the flame. Since the flame location may not necessarily be consistent between all calibration flames and unseeded flame measurements, the NO signals are all shifted such that NO production occurs at a consistent pixel location. Then, the scale factor (Appendix A) is applied to convert the  $x$ -axis of the graph from pixels to mm. Fig. 4-7 displays the initial raw flame measurements (4-7a) and the final processed measurements in concentration and axial position (4-7b).

The final, quantitative fluorescence signal can be seen in Fig. 4-8 in the context of the stagnation flame geometry. The axial location of the plot refers to position along the  $y$ -axis, centred at the flame front.

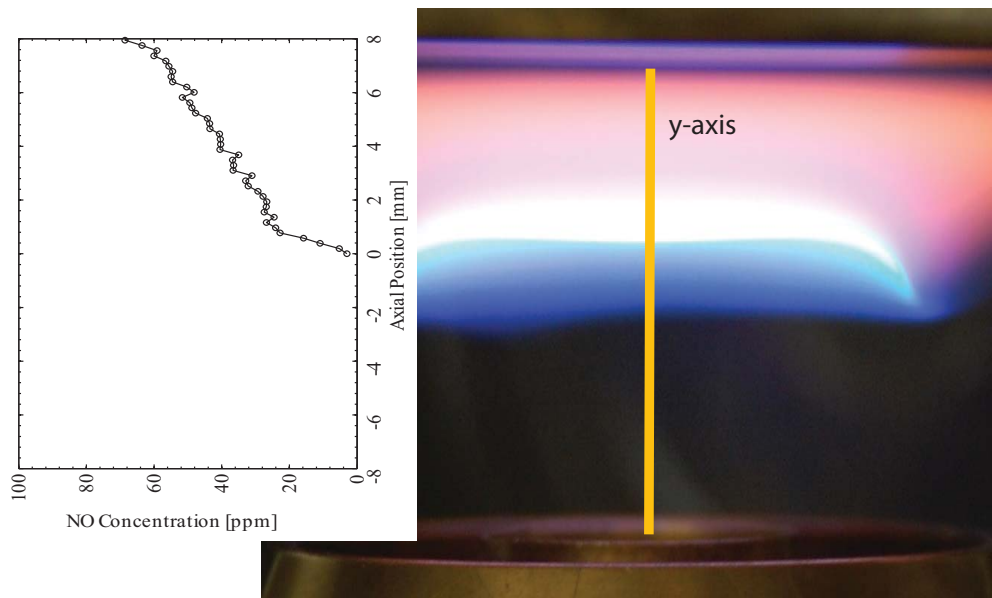


Figure 4-8: *n*-butanol flame  $\phi=1.0$  with the corresponding NO concentration plot, illustrating the spatial *y*-coordinate.

## CHAPTER 5 Results and Discussion

### 5.1 Stagnation Flame Velocity and Reactivity

The centreline velocity profiles were obtained for all fuels and experimental conditions using PIV. These velocity profiles can not only provide experimental boundary conditions to be used in simulations, but can also provide valuable information regarding the reactivity of each flame. Experimental stagnation flame velocity profiles can be compared to simulated profiles to judge the ability of the kinetic model to accurately model the flame chemistry.

#### 5.1.1 Experimental Stagnation Flame Velocity Profiles

The centreline velocity profiles are shown in Figures 5–1 to 5–4. Each profile consists of a parabolic drop in exit velocity (right side of plots) until a local minimum, designated as the reference flame speed  $S_{u,\text{ref}}$ , is reached. Physically, this is where the stagnation flame has stabilized between nozzle exit and stagnation plane. The flow is then accelerated and expanded through the hot flame, leading to a large spike in centreline velocity. Post-flame, the centreline flow will slow down to zero axial velocity against the plate and the flow is forced out radially.

In the PIV experiments, the flame position at each equivalence ratio was kept constant for each fuel. Thus, for the same fuel, a comparison can be made between  $S_{u,\text{ref}}$  of different  $\phi$  since  $S_{u,\text{ref}}$  is coupled to flame position. Photos of *n*-butanol and *n*-butane stagnation flames, seen in Fig. 5–5, illustrate the difference in appearance

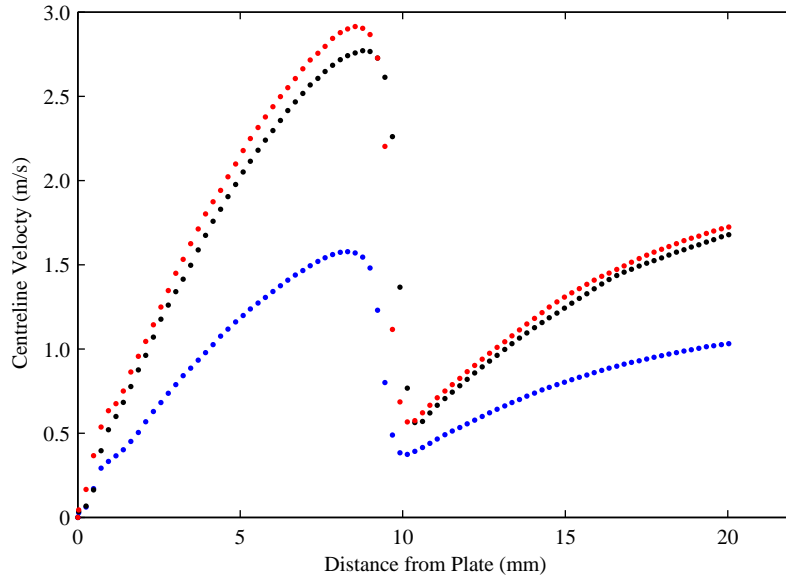


Figure 5–1: Centreline velocity profiles of *n*-butanol flames:  $\phi=0.8$  (blue),  $\phi=1.0$  (black),  $\phi=1.3$  (red)

between alkane and alcohol flames. This is reflected in the relative difference in flame speeds and combustion kinetics. Visually, butanol flames display more soot formation, seen in the orange halo in the post-flame zone. Butanol sooting characteristics, caused by hydrocarbon growth processes, are noted in previous papers [37, 43].

### 5.1.2 Velocity Profile Comparisons to Simulation

In literature, the laminar flame speed,  $S_f^0$ , is an oft-discussed combustion characteristic which describes the unstrained burning rate of a flame at defined experimental conditions. The laminar flame speed can be linked directly to the reactivity of the fuel-air mixture and thus provides a single quantity which can represent the overall chemical kinetics of the reaction. Once  $S_f^0$  is obtained experimentally, a kinetic

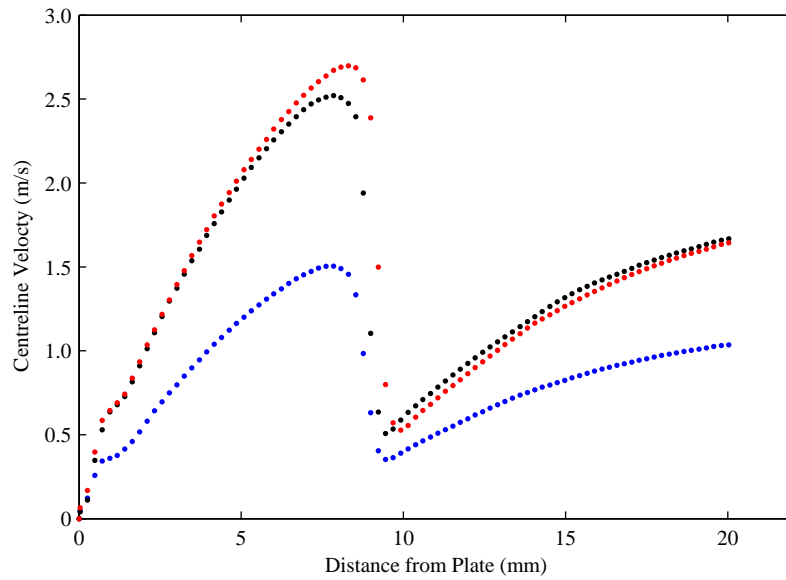


Figure 5-2: Centreline velocity profiles of *iso*-butanol flames:  $\phi=0.8$  (blue),  $\phi=1.0$  (black),  $\phi=1.3$  (red)

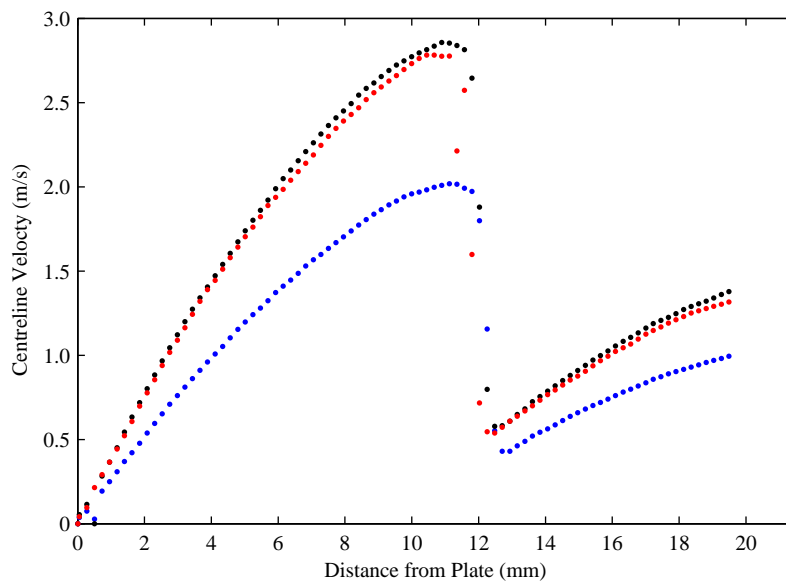


Figure 5-3: Centreline velocity profiles of *n*-butane flames:  $\phi=0.8$  (blue),  $\phi=1.0$  (black),  $\phi=1.3$  (red)

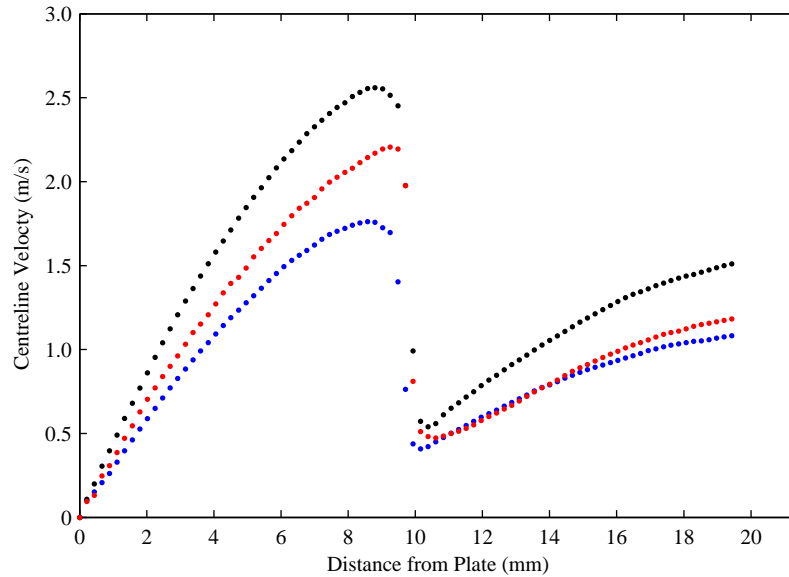


Figure 5–4: Centreline velocity profiles of *iso*-butane flames:  $\phi=0.8$  (blue),  $\phi=1.0$  (black),  $\phi=1.3$  (red)

mechanism is typically used to simulate the same value – the differences between the predicted and measured  $S_f^0$  are analysed and used to improve that kinetic model.

$S_{u,\text{ref}}$  represents the strained burning rate of the flame in the stagnation flame geometry from which a non-linear extrapolation is required to obtain  $S_f^0$  [28, 60]. It is possible to avoid this extrapolation, however, by simulating the stagnation profile directly, using a different reactor model offered by Chemkin [18]. Though this method increases the computational cost of simulation, direct stagnation flame simulation removes the uncertainty associated with the non-linear extrapolation technique while still providing similar insight into the reactivity of the flame. Thus, obtaining the velocity profiles of these flames provides a valuable experimental target for continued development of kinetic mechanisms.



Figure 5-5: Photo of *n*-butanol (left) and *n*-butane (right) stagnation flames:  $\phi=0.8$  (top),  $\phi=1.0$  (middle),  $\phi=1.3$  (bottom)

The simulations were performed using experimentally obtained values for flow and stagnation plane temperature, radial gradient of velocity, inlet velocity and distance from the plate as boundary conditions. See Appendix E for a table of values used for simulation boundary conditions.

Figure 5–6a displays a comparison between the chosen model for *n*-butanol, the Sarathy-Dagaut mechanism, and the experimental data obtained from PIV for the same fuel. Table 5–1 illustrates the difference between measured and predicted  $S_{u,\text{ref}}$ . The model prediction appears to be adequate for the lean flame, but significantly under-predicts the stoichiometric and rich flames.

In all cases, the under-prediction of  $S_{u,\text{ref}}$  by the mechanism indicates that the model may require a modification to its rate constants to increase reactivity for *n*-butanol combustion. This is consistent with the study by Veloo et al. [60] which also found the Sarathy-Dagaut to under-predict the reactivity of premixed counterflow *n*-butanol flames. In [60], it was found that the Sarathy-Dagaut model under-predicts the laminar flame speed of butanol by 10-20% over a wide range of  $\phi$ . It should be noted that  $\Delta S_{u,\text{ref}}$  between experiment and simulation will also result in the same  $\Delta$  for  $S_f^0$  [6]. The similarity of under-prediction seen between Veloo et al. and this study

Fuel	$\phi$	Exp. $S_{u,\text{ref}}$ (cm/s)	Sim. $S_{u,\text{ref}}$ (cm/s)	% difference
<i>n</i> -butanol	0.8	37.34	34.85	6.7
	1.0	54.90	47.68	13.2
	1.3	56.02	44.99	20.0
<i>n</i> -butane	0.8	41.96	43.81	4.4
	1.0	56.40	54.79	2.9
	1.3	53.41	45.89	14.1

Table 5–1: Experimental  $S_{u,\text{ref}}$  compared to simulations

strongly suggests that a modification to the mechanism is necessary. Furthermore, the similarity of results despite different methods of evaluating  $\Delta S_f^0$  validates the current findings.

A plot contrasting experiments and simulations is shown for the corresponding alkane fuel, *n*-butane (Fig. 5–6b). By again comparing the  $S_{u,\text{ref}}$  for each equivalence ratio, it can be seen that the mechanism used here, USC\_Mech V.II, performs better than the Sarathy-Dagaut model at predicting experimental profiles.

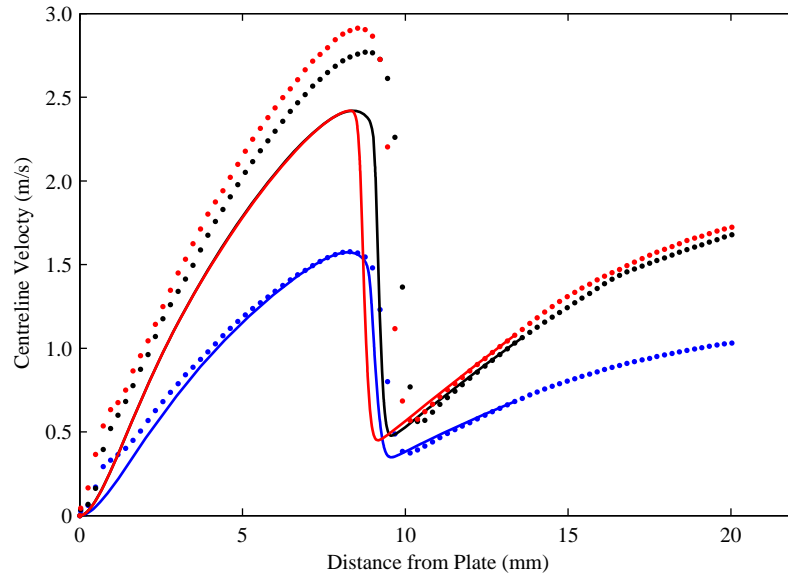
Again referring to Table 5–1, USC\_Mech V.II demonstrates good agreement in velocity profiles of lean and stoichiometric butane flames – there is less than 5% difference between predicted and measured  $S_{u,\text{ref}}$ . The mechanism, however, does not appear to be able to predict the rich scenario accurately. There is a significant under-prediction of 14%, suggesting that the mechanism may need to be adjusted for rich flames. Further study must be conducted to draw more detailed conclusions about these modifications as it is not the primary goal of this thesis to study the relative reactivity of butanol/butane with respect to the simulated models.

## 5.2 NO Production in Stagnation Flames

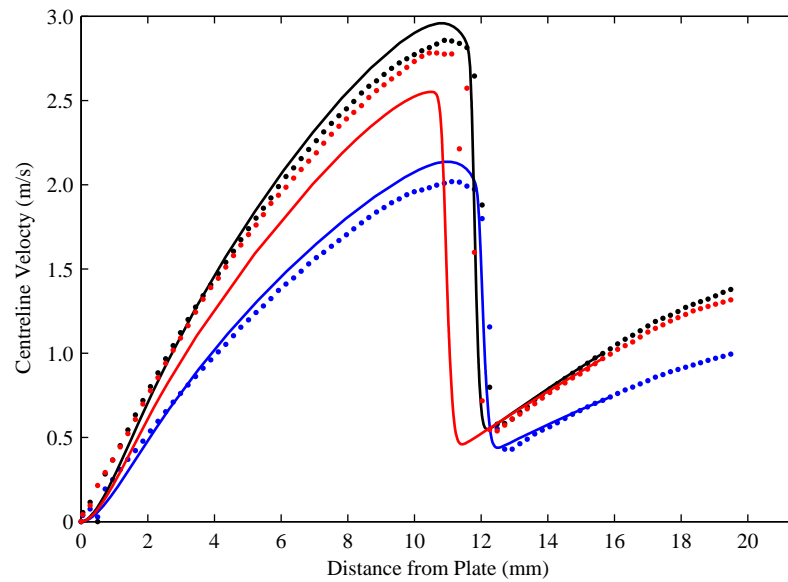
### 5.2.1 Calibration Curves

The calibration curves determined through the calibration technique performed in Run 2 Section 4.4 are shown in Fig. 5–7. The linear fit used in all plots shows a good fit to the measured data, indicating that the calibration measurements are reliable.

While all the calibration curves are valid and were used to quantify their respective unseeded NO profiles, the uncertainty in the calibration technique can be



(a) *n*-butanol / Sarathy-Dagaut mechanism



(b) *n*-butane / USC\_Mech V.II mechanism

Figure 5–6: Comparison of centreline velocity profiles (dots) to simulations (lines):  $\phi=0.8$  (blue),  $\phi=1.0$  (black),  $\phi=1.3$  (red)

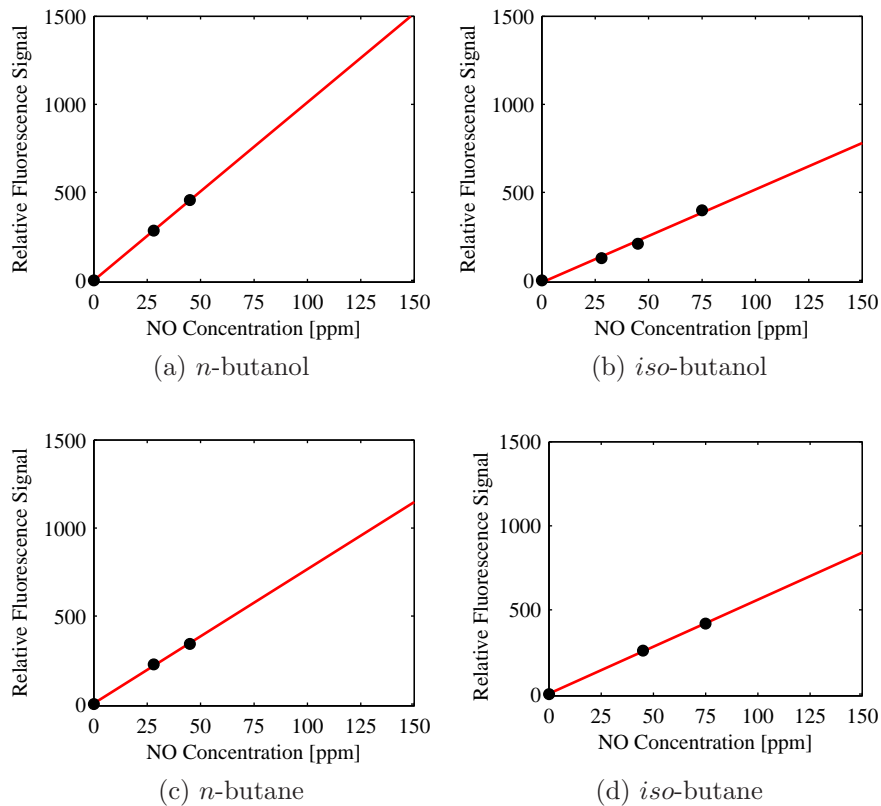


Figure 5-7: Calibration curves for the four fuels: linear interpolation (line) of calibration points (●)

reduced if more calibration points are taken. Three calibration points are the minimum number of points required to define the line and create a linear fit to the data. We would thus expect higher amounts of uncertainty than if more points were used. The addition of more measurements, either at different concentrations or repeated at the same seeding concentration, will increase confidence in the fit. Future measurements made with the calibration curves will include higher levels of NO seeding in addition to more calibration points.

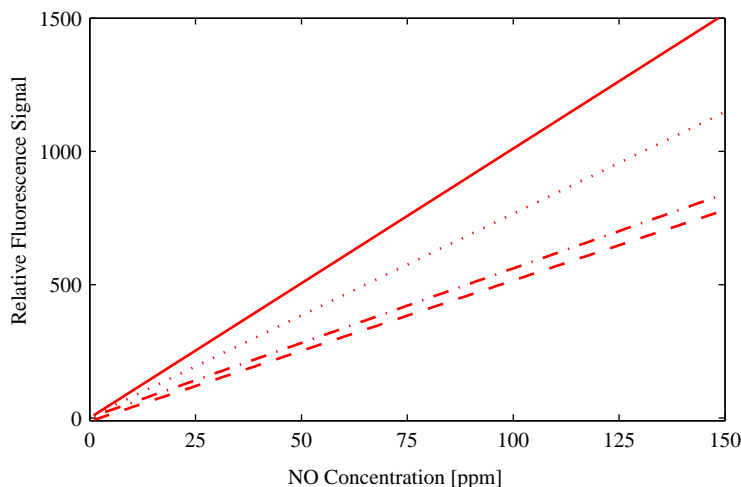


Figure 5-8: Comparison of calibration curves: *n*-butanol (solid), *iso*-butanol (dash), *n*-butane (dot), *iso*-butane (dash-dot)

When the calibration curves are plotted together (Fig. 5-8), the large variations in slope between fuels become quite apparent. There does not appear to be a relation between the slope of the curve and the fuel type – *n*-butanol and *iso*-butanol are similar fuels but display significantly different slopes. It is possible that the change in slope is caused by an increase in excitation laser intensity, however this was carefully controlled and monitored during the experiments. The slope difference could be caused by an effect of dye degradation and the ability of the dye to excite the same number of NO molecules after it has been used over several days of experiments. While this may be a viable explanation, it does not explain the drop in slope between *n*-butane and *iso*-butane between which old dye was replaced with fresh dye.

Wavelength drift in the dye laser is the most likely explanation of this changing calibration slope. Despite efforts to find the peak excitation wavelength with an excitation scan at the beginning of each day, it may still be possible that the selected

wavelength is not the optimal. A small change in excitation wavelength could result in a significant reduction in the resulting fluorescence – recall from Figure 3–5 that any minor shift in wavelength off the excitation peak will yield a major loss of LIF signal. Since the excitation scan conducted for each fuel was subjective, it is certainly possible that the most ideal excitation wavelength was not found during the scan. The excitation scan procedure can be improved by creating an objective measure of a ‘peak’ on-line signal. See Appendix F for additional recommendations.

### 5.2.2 Experimental NO profiles for Butanol and Butane Flames

Figure 5–9 displays experimental results from the NO-PLIF of *n*-butanol, *iso*-butanol, *n*-butane and *iso*-butane at the three equivalence ratios  $\phi = 0.8, 1.0$  and  $1.3$ . The plots illustrate the effect of equivalence ratio change on the shape and absolute concentration of the NO profile. Note that the flames have been shifted such that the flame front, and thus NO formation, begins at the axial position of zero.

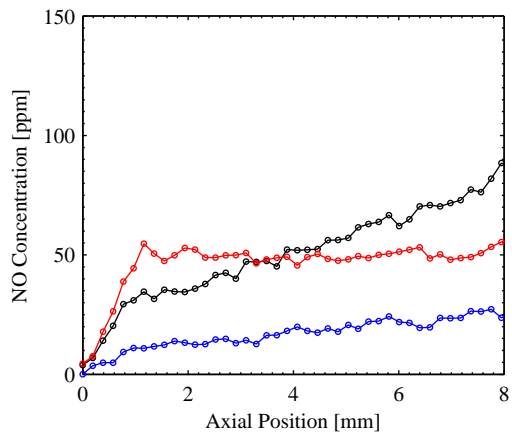
All four fuels display consistent trends between flames - the lean flame produces significantly less NO than the rich and stoichiometric cases, while  $\phi = 1.0$  produces less NO initially through the flame front but increases with distance from the flame. The rich flames typically produce the most NO immediately through the flame but do not produce a significant amount in the post-flame region.

A closer look at the curve shapes in Fig. 5–9 can reveal information about the on-going NO chemical reactions. Each flame plot displays a two-part structure, which indicates that a different formation pathway is dominant in each region. Moreover, the difference in the profile structures between equivalence ratios suggests that the

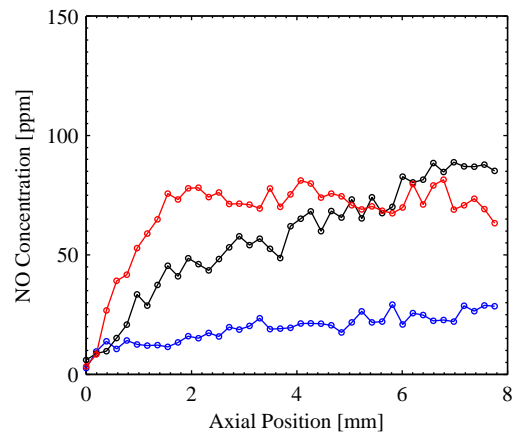
importance of each formation pathway changes with  $\phi$ . The location of a measurement in the post-flame zone can be related to the residence time spent within the flow. The amount of time spent in the flow is equal to the distance travelled away from the flame divided by the flow velocity. Thus, slow reactions will change the measured concentration gradually with downstream post-flame position, while fast reactions will cause sharp increases in concentration with respect to position.

From literature, it is known that the prompt-NO pathway occurs quickly within the flame zone and is most sensitive to flame/fuel chemistry, while thermal-NO production is slower and is fuel chemistry independent [38]. In the context of the experimental results, this would indicate that the prompt pathway is primarily responsible for the initial sharp rise of the NO profile due to its location within the flame zone and high rate of production. The width of the flame zone can be determined using the prompt-NO slope as an indicator – it appears that for  $\phi = 0.8$ , the flame zone spans between 0 and  $\sim 1$  mm in axial position. For  $\phi=1.0$  and 1.3, however, the flame zone is thicker, approximately 1.5 mm wide. The thickening of the flame as fuel ratio increases is well observed in [2].

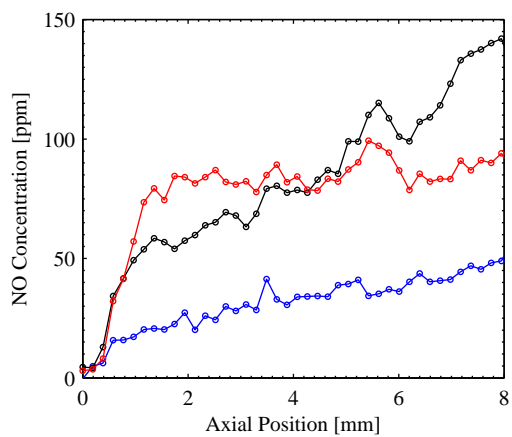
The thermal pathway appears to dominate the burned-gases region of the profile ( $\geq 1.5$  mm axial position). The slope of the curve in this profile indicates a rate of reaction that is dependent on flame temperature: flames at  $\phi = 1.0$  (black in Fig. 5–9) burning with a higher temperature display a steeper slope than flames at  $\phi = 0.8$  (blue). For all fuels, the  $\phi = 1.3$  flame (red) displays minimal amounts of thermal-NO production even though the temperature of the post-flame region is relatively high.



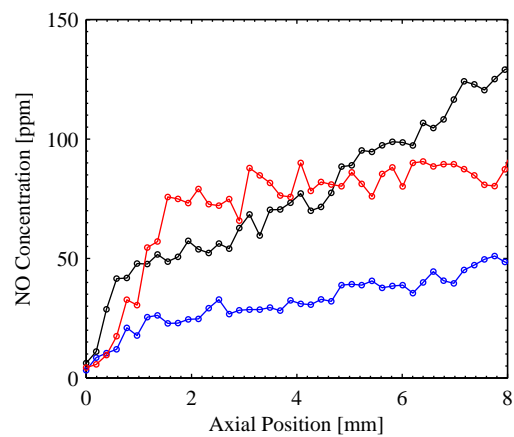
(a) *n*-butanol



(b) *iso*-butanol



(c) *n*-butane



(d) *iso*-butane

Figure 5–9: NO concentration profiles for the four fuels:  $\phi=0.8$  (blue),  $\phi=1.0$  (black),  $\phi=1.3$  (red)

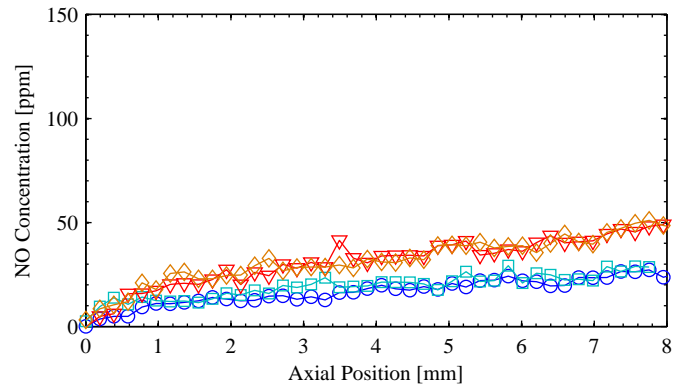
Due to the lack of O-atoms in the flame and post-flame zones, the oxygen-consuming thermal-NO reactions are not significant at rich conditions [38].

These findings are consistent with Marques et al. [36], who also found that the thermal-NO pathway dominated at the stoichiometric condition, while prompt-NO was dominant in for rich flames. Marques et al. also displayed ethanol NO concentration profiles very similar in shape to Fig. 5–9, further supporting the validity of the results obtained in this study.

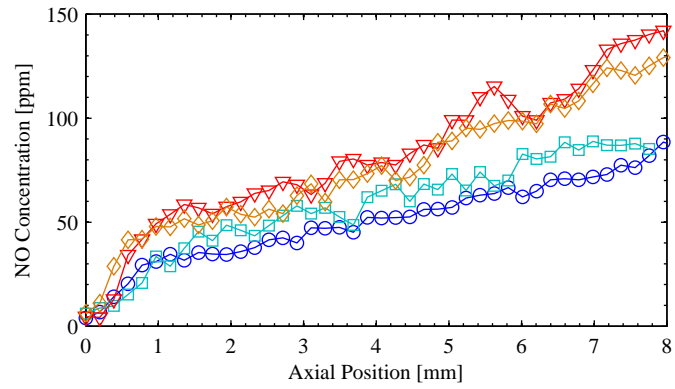
When the NO profiles of the fuels are separated by equivalence ratio, it is possible to study the effects of differing combustion chemistry on NO formation. Figure 5–10 not only illustrates the difference in the overall NO formation between alkane-type fuels and alcohol-type fuels, but also between isomers of the same fuel type.

Figure 5–10a, which plots the NO profiles of all  $\phi = 0.8$  flames, shows a collapse of profiles between isomers – there is negligible difference in NO formation between *n*- and *iso*-butanol and between *n*- and *iso*-butane. There is, however, a clear distinction in concentrations between alkane and alcohol fuels. In the post-flame region, the NO produced by alcohol fuels at this lean condition is generally half of that produced by alkane fuels. Within the same region, the slope of the butane concentration profiles are also slightly steeper than the butanol profiles, indicating a higher flame temperature and more NO generated by the thermal pathway.

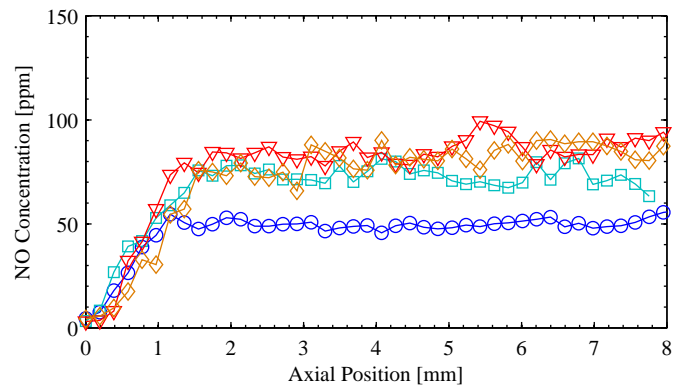
Fig. 5–10b displays the same collapse of isomeric profiles for stoichiometric flames – given the experimental scatter of the data points, there appears to be no significant difference in concentration profiles between isomers of the same fuel



(a)  $\phi = 0.8$



(b)  $\phi = 1.0$



(c)  $\phi = 1.3$

Figure 5–10: NO concentration profiles plotted separately as a function of equivalence ratio: *n*-butanol (blue  $\circ$ ), *iso*-butanol (teal  $\square$ ), *n*-butane (red  $\nabla$ ) and *iso*-butane (orange  $\diamond$ )

type. Although still within the experimental scatter of the *n*-butanol data, the *iso*-butanol profile appears to display slightly higher average NO production with more prompt-NO production through the flame zone. Comparing alcohols with alkanes, the butanes again produce more thermal-NO resulting from higher post-flame temperatures. In this plot, the butanes are also seen clearly to produce greater amounts of NO through the flame zone, indicating more NO formation via the prompt-NO pathway.

The trends of the lean and stoichiometric cases are not followed for the rich condition, as seen in Fig. 5–10c. The indication of divergence between *n*-butanol and *iso*-butanol as seen for  $\phi = 1.0$  has become much more pronounced for  $\phi = 1.3$ . The significantly lower NO-formation of *n*-butanol occurs exclusively due to the prompt-NO pathway, indicating a difference in concentrations of intermediates leading to prompt-NO generation such as  $\text{CH}_3$ . Further research is necessary to verify the differences in combustion chemistries between fuels with respect to NO production.

In general, the collapse of NO concentration profiles of the butanol isomers and the butane isomers for lean and stoichiometric flames is remarkable given that the data sets were taken on separate days, with different beam shapes and unique calibration curves. This observation strongly indicates that this isomeric collapse is representative of the NO-formation by the flames and that the employed corrections and calibrations are applied correctly. Butanol fuels conclusively produce less NO than butane fuels in a direct experimental comparison. Comparisons between

simulated ethanol and hydrocarbon NO concentrations have been conducted by Saxena and Williams [52], finding a similar difference in overall formation. This study provides the first direct experimental comparison of spatially resolved NO profiles between alcohol and alkane fuels.

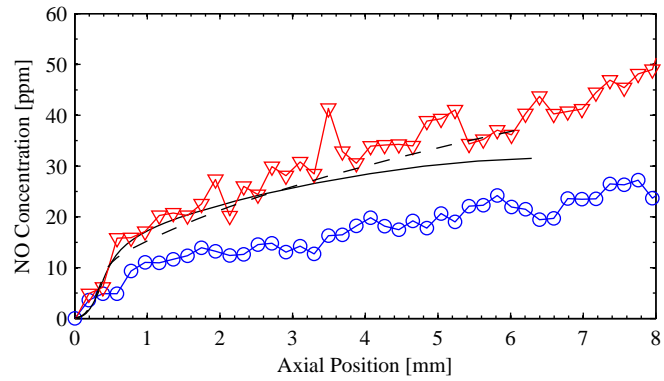
### 5.2.3 NO Concentration Profile Comparisons

NO profiles generated in the simulations were plotted against experimental data in Fig. 5–11. As described in previous sections, the NO<sub>x</sub> reactions utilized here were taken from GDF\_kin3.0.

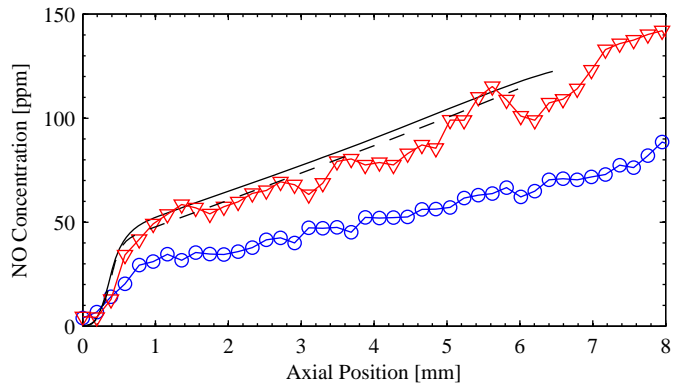
Fig. 5–11a shows a good prediction of the lean experimental *n*-butane NO profile by USC\_Mech V.II. The same cannot be said for the prediction of *n*-butanol by the Sarathy-Dagaut mechanism. The butanol mechanism appears to over-predict the NO produced through the prompt-NO pathway while maintaining a thermal-NO slope in the post-flame region similar to the experiment.

Fig. 5–11b also shows a very good prediction of the  $\phi = 1.0$  *n*-butane NO profile by USC\_Mech V.II. The simulation is able to accurately capture both the prompt-NO formed through the flame as well as the thermal-NO in the post-flame. Once again, the Sarathy-Dagaut mechanism fails to accurately predict the *n*-butanol NO concentration profile, with an over-prediction in both the flame zone and the post-flame zone.

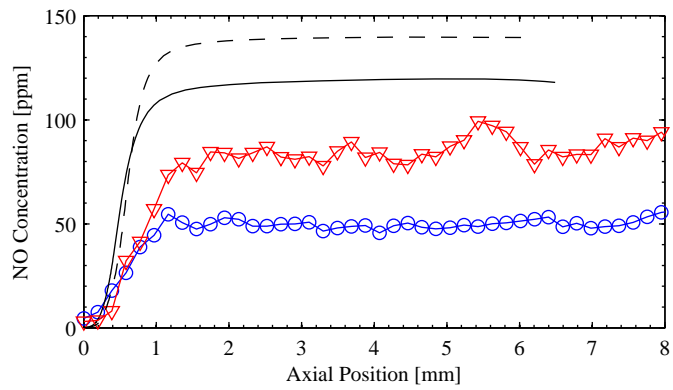
In both  $\phi = 0.7$  and 1.0 cases, the butanol mechanism has predicted a NO profile that is similar to butane. This indicates that the butanol mechanism is able to capture the formation of NO for an alkane fuel but not of an alcohol fuel. It



(a)  $\phi = 0.8$



(b)  $\phi = 1.0$



(c)  $\phi = 1.3$

Figure 5–11: Comparison of NO concentration profiles to simulations: *n*-butanol (blue  $\circ$ ) with Sarathy-Dagaut mechanism (solid) and *n*-butane (red  $\nabla$ ) with USC\_Mech V.II (dash)

may be concluded, then, that there are significant chemical kinetic effects occurring specifically in butanol flames that are not captured by the model.

At the final equivalence ratio  $\phi = 1.3$ , neither mechanism is able to accurately predict the experimental profiles. For this case, although still significantly over-predicting total concentration, the butanol mechanism predicted a lower NO profile than butane. It appears that any shortcomings of the mechanisms with respect to combustion and NO formation chemistry are exaggerated in the rich case, where thermal-NO production is negligible. While both models require modification to adequately capture the reduced NO concentration at  $\phi = 1.3$ , USC\_Mech V.II combined with the NO<sub>x</sub> sub-mechanism appears to predict lean and stoichiometric cases well. The failure of both models to predict NO formation at rich conditions could stem from the corresponding failure of the mechanism to predict the reactivity and stagnation flame speed. It is possible that a poor prediction of intermediate species concentrations or reaction rates could also lead to both an over-prediction of prompt-NO formation and an under-prediction of flame speed. Further studies in kinetic modelling must be performed under rich conditions to confirm or refute the above hypothesis.

#### 5.2.4 Standard Deviation

The experimental scatter of the data was investigated by calculation of the standard deviation in the raw PLIF signal which was then propagated through all correlation processes. Figure 5–12a shows a plot of *n*-butanol data from Fig. 5–9a with the calculated error bars. For each raw PLIF image, the width of the first fluorescence line was averaged at every axial position.

The standard deviation of each image, or sample, is calculated:

$$\sigma_{sample}(\bar{x}) = \sqrt{\frac{1}{N-1} \sum_{i=1}^N (x_i - \bar{x})^2}$$

where  $\bar{x}$  is the mean of all samples. The standard deviation of the mean measures the variability of the mean itself:

$$\sigma_{mean} = \frac{1}{\sqrt{N}} \sigma_{sample}$$

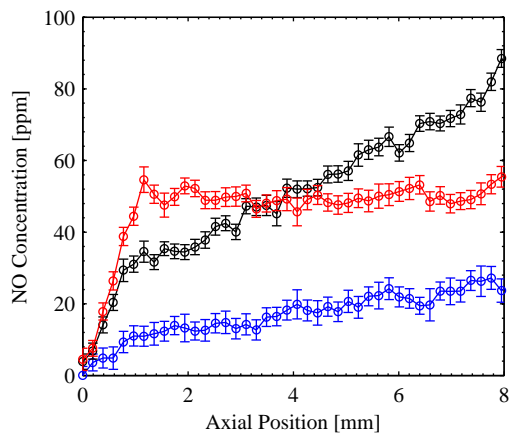
Two standard deviations from the mean were then calculated over the 500 raw images and plotted with the experimental data as error bars giving a 95% confidence interval.

At all equivalence ratios, the size of the error bars remain relatively small and consistent while the variations in NO concentration profiles occur at a larger amplitude. Indeed, Fig. 5–12b shows that the  $2\sigma$  values for standard deviation are consistently under 5 ppm. This indicates that the fluctuations seen in the profiles are a result of uneven intensity distribution of the exciting laser sheet and not a result of noise in the collection apparatus. Normalization of the PLIF signal by beam distribution (Section 4.3) appears to not be completely effective at removing these variations, indicating further improvements to the experiment and method are necessary to remove them.

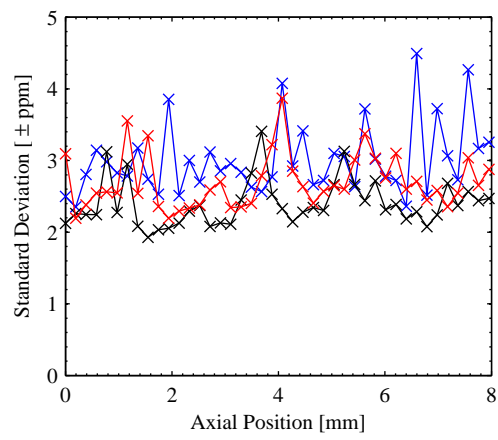
It should be noted that, despite the relatively low standard deviation from the mean displayed, the standard deviation of each image is much higher. Because the raw images are essentially composed of single-photon type events (a single photon is collected and amplified to fill a pixel), the images contain a map of light and dark

pixels which may not represent the actual fluorescence occurring unless averaged over multiple images. The calculated standard deviation of a small sample will be high because the excited band of fluorescence will contain both light and dark pixels (refer to Fig. 3-7(right)). When averaged over many images, however, the fluorescence signal can be seen clearly (Fig. 3-7(left)).

From an analysis of the random error of the measurements, it can be concluded that the developed PLIF measurement methods have the ability to resolve the trends observed in the Sections 5.2.2 and 5.2.3. It should be noted that this analysis only illustrates the random error in the captured images – the uncertainties in certain aspects of the stagnation flame burner (flow composition  $\phi$  and PIV processing) have not been accounted for. Systematic uncertainties with excitation (laser power and intensity distribution fluctuations between measurements) are difficult to quantify and were also not analysed.



(a) NO profile with plotted error bars



(b) Standard deviation in raw data

Figure 5–12: Standard deviation of *n*-butanol flames:  $\phi=0.8$  (blue),  $\phi=1.0$  (black),  $\phi=1.3$  (red)

## CHAPTER 6

### Conclusions

The on-going study of NO<sub>x</sub> emissions from combustion sources is important, given the struggle to control air pollution worldwide. This study is motivated by the potential reduction in NO<sub>x</sub> emissions from next generation biofuels like butanol and their advantages over conventional fossil fuels. A planar laser-induced fluorescence apparatus was constructed to measure quantitative concentrations of nitric oxide from the combustion of premixed fuels in a stagnation flame geometry. Measurements of NO generated by laminar flames offer a fundamental look at the chemistry of butanol combustion and the effects of fuel chemistry on NO production. Additionally, particle-image velocimetry was performed to determine the centreline velocity profile, from which comparisons can be made between kinetic models and experiment.

It was found, through comparison of simulated and experimental velocity profiles, that the Sarathy-Dagaut mechanism significantly under-predicts the reference flame speeds of *n*-butanol at all tested equivalence ratios. The velocity profiles of *n*-butane at lean and stoichiometric  $\phi$  were well predicted by USC\_Mech V.II, but the rich case was under-predicted.

The experimental NO profiles for *n*-butanol, *iso*-butanol, *n*-butane and *iso*-butane showed consistent trends between equivalence ratios. Lean and stoichiometric NO profiles showed a two-stage structure, where the prompt-NO pathway is dominant in the flame and the thermal-NO pathway is dominant in the post-flame region.

Rich NO profiles contained only prompt-NO production and negligible thermal-NO production. The NO concentration profiles at lean and stoichiometric  $\phi$  showed a collapse between isomers of the same fuel type, indicating negligible difference in overall NO generation over the experimental domain. Compared to the butanes, the butanol fuels displayed significantly lower prompt-NO production and similar thermal-NO production. For rich  $\phi$ , *n*-butanol displayed lower NO production as compared to the other three fuels, suggesting that the combustion chemistry in *n*-butanol offers lower NO-prompt generation.

This is the first study to compare experimentally quantitative NO formation of alcohol and alkane flames. Overall, butanol fuels produce significantly less NO than butane fuels, particularly through the prompt-NO pathway. This finding indicates that the reduction in NO stems directly from differing fuel chemistry. Thus, if only the combustion chemistry is considered, it appears that alcohol biofuels can offer fundamentally lower NO<sub>x</sub> production than conventional alkane fuels.

*n*-Butanol simulations of NO profiles proved to have poor agreement with the experiments, over-predicting the production at all equivalence ratios. The similarity of slope in the post-flame region between model and experiment indicates that the thermal-NO pathway is adequately predicted. The disparity in NO formation occurs in the flame zone via the prompt-NO pathway, suggesting that the chemical kinetics in the mechanism require improvement. Conversely, the *n*-butane NO profile simulations performed well when compared with the experiment. The mechanism gave good agreement for lean and stoichiometric equivalence ratios, but significantly over-predicted the rich case. This is, perhaps, not surprising given the failure of

the mechanism to predict the reactivity of rich flames in the velocity profile simulation. In a similar trend, an under-prediction of reference flame speed by the Sarathy-Dagaut mechanism is also seen to lead to an over-prediction of prompt-NO production. This could possibly stem from the inability of the kinetic mechanism to accurately predict the pool of intermediate species formed in the flame zone.

This study offers new experimental data to aid in further improvements in kinetic modelling of butanol and butane combustion. Additionally, it provides validation of the NO<sub>x</sub> sub-mechanism, GDF\_kin3.0, for further improvements in the study of NO chemistry of oxygenated and longer-chained fuels. The fundamental study of both NO<sub>x</sub> chemistry and alternative fuel combustion continue to be essential in the efforts to control air pollution and reduce fossil fuel dependence.

## Appendix A: Obtaining Spatial PLIF Measurements

Significant time and effort was spent on experimental set-up and troubleshooting for the fluorescence collection system. While it was not difficult to obtain a signal from NO fluorescence, ensuring that this signal is properly resolved and focused required a great deal of time.

The collection optics set-up underwent several iterations before the design was finalized. The key to aligning and optimizing the optical set-up was realizing that the focusing of the optics must be done while the spectrograph is measuring at the desired fluorescence wavelength. For all experiments, the spectrograph was centred at 246 nm. The internal reflection mode of the spectrograph (0 nm) cannot be used to focus the optics for UV signal collection - the focal lengths are significantly different. It was found that the focusing of the optics was best done while seeding the collection volume with NO and exciting with the UV laser.

A card with small holes was employed as a method of selectively allowing parts of the laser sheet through, thus creating a spatial aspect in the excitation sheet. Light beams emanating through the holes of the card excited bands of NO molecules, while the areas where the light sheet was blocked were left unexcited. The optics were optimized to provide the best amount of sharpness and resolution to the excited areas. Fig. 6-1 shows NO-PLIF of illuminated areas during focusing and alignment.

See Fig. 6-2 for detailed dimensions of the set-up. Spatial measurements were not possible without the addition of a second iris diaphragm in front of the collection lens ( $f = 15$  mm). Prior to its addition, the signals that were received by



Figure 6-1: An image of the focusing for to determine scale factor, averaged for 500 images.

the spectrograph and ICCD camera were blurred and non-resolved. With the signal iris, the amount of diffuse, scattered light from the NO fluorescence outside of the collection volume was cut down, allowing for better resolution within the  $V_c$ . An optimal location of the iris with respect to the nozzle and collection lens was found through trial and error.

Once closing the iris began to yield spatial signals, it became much easier to move the collection lens to its focal point. With the collection lens in an ideal location away from the spectrograph slit, the lens was moved up and down such that the entire laser sheet can be captured within one image. The final magnification was less than 1:1. The optimal focal length between the ICCD camera and the spectrograph was found in a similar way – the card was used to excite lines of seeded NO. The camera was moved until an optimal focus was found where the spots of excited NO were the smallest and best defined.

The final magnification of the camera image can be determined by comparing the final captured image to the size of the holes in the card and the distance between

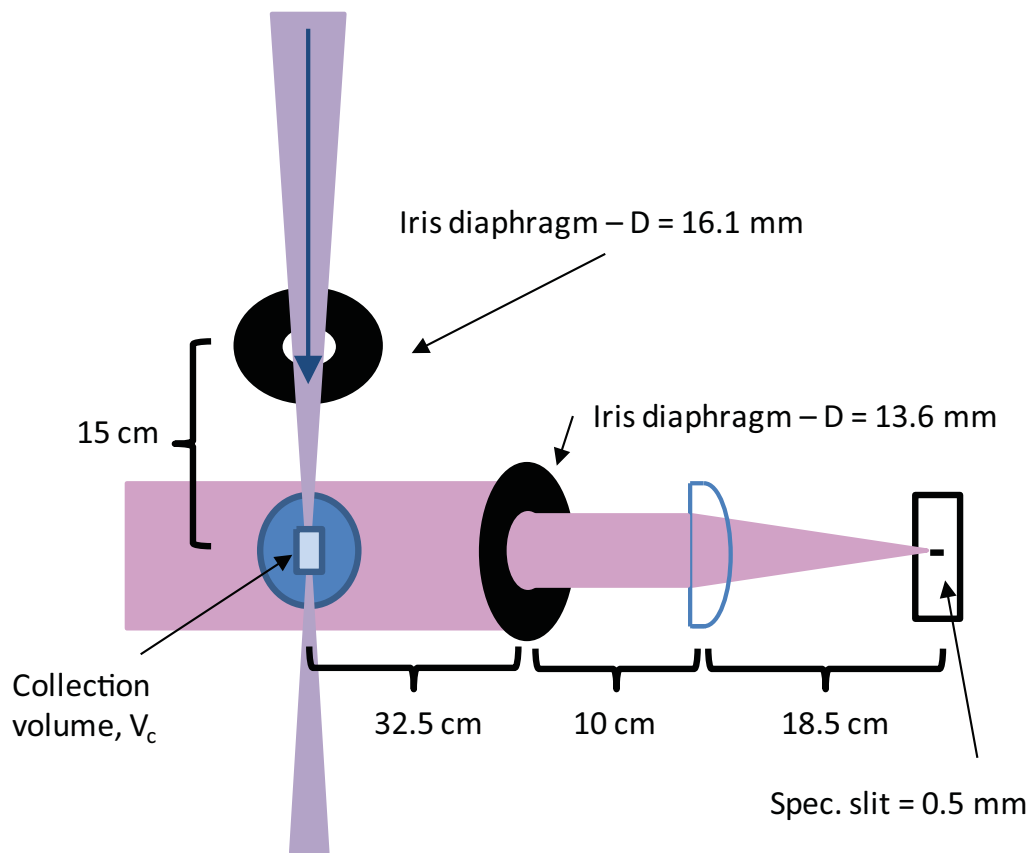


Figure 6-2: Detailed dimensions and settings of the collection optics

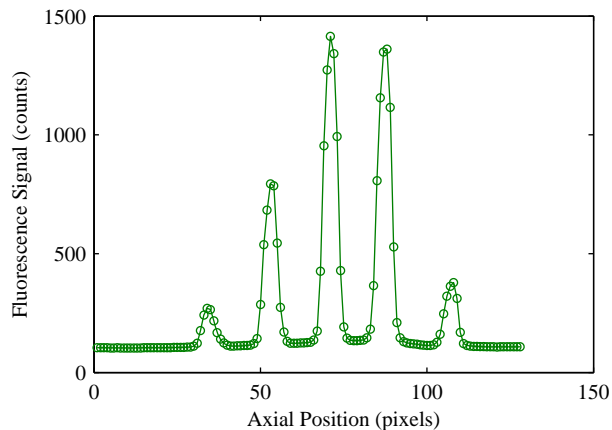


Figure 6-3: Vertical profile of fluorescence - test of magnification. Flow was seeded with NO molecules and excited at pre-defined points.

holes. The vertical profile along the 1st fluorescence line ( $\sim 236$  nm) was taken and plotted in Fig. 6-3, with the horizontal axis representing the spatial location between the top and bottom edges of the laser sheet. It is expected that the laser lines will diverge when passing through the holes and thus appear to give a larger hole width and a reduced distance between holes. Refer to Appendix F for additional recommendations.

The full-width half-peak measurement was taken for each of the peaks for 1st fluorescence line and the fluorescence profile is plotted in Fig. 6-4. The ratios of the measured hole widths and distances were almost identical when compared to this figure. The hole diameter was measured via fluorescence to be approximately equal to the caliper measurement. The spatial magnification was calculated to be 0.194 mm/pixel.

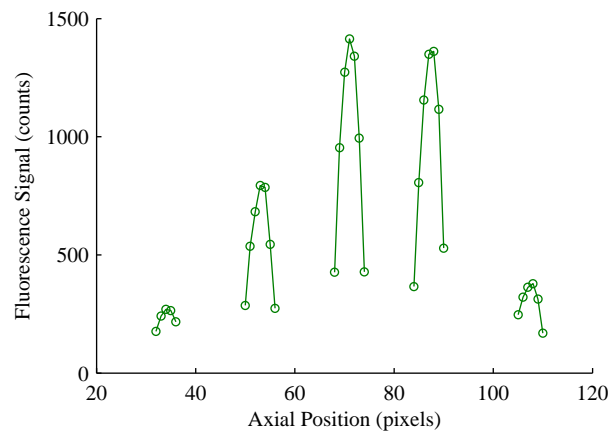


Figure 6-4: Magnification test plotted at 50% maximum.

## Appendix B: Maintenance and Continued Operation of the PLIF/Stagnation Flame System

### Laser and Optics

All optical equipment (lenses, prisms) should be kept clear of dust and cleaned periodically. A plastic bag was used to cover the lenses for overnight storage. The camera-spectrograph connection was kept intact through all experiments. The spectrograph slit cover should be replaced when the camera is not needed to minimize stray light and dust entering the spectrograph.

The dye laser and Nd:YAG pump laser were both tuned for optimal operation by a technician from Newport Corp. Minimal changes were made to both lasers after they were tuned. The laser dye solution was changed periodically when the dye laser is no longer able to reach the desired power level. The laser dye was found to degrade proportionally to the pumping laser power (and dye laser power) – higher pump energies led to faster degradation of the dye. At a UV laser sheet power of 0.5 mJ, the dye needed to be changed within  $\sim 15$  hours of total operation.

### Laser Dye and Handling

Coumarin 450 laser dye, purchased from Exciton, was used to produce a beam of  $\sim 452$  nm which was then frequency-doubled to the excitation wavelength of NO. The dye solution consisted of the Coumarin dye and an appropriate amount of 100% pure ethanol solvent. There were two required concentrations of dye solution - one for the resonator/pre-amplifier dye cell (0.2 g/L) and the other for the amplifier dye cell (0.0667 g/L). The appropriate amount of dye solute was measured using an

electronic scale and mixed with ethanol measured with a volumetric flask. The dye solution was mixed for an hour on a stir plate. Spare dye was stored in 4 L amber glass jugs away from direct light.

The laser dye solutions were carefully filled into their respective dye pump flasks. The dye pumps were run for a period of time to remove bubbles. The flasks should be reasonably full when the pumps are in operation, but not full enough to overflow when hoses/dye cell are emptied back into the flask. Extra care was taken when removing the dye cells from the housing in the laser. The connection between the hose and the dye cell is fragile and has been known to break. Fingerprints on the dye cell were cleaned off with solvent and lens cleaning paper before the cell was re-inserted into the laser. Appropriate hand, body and eye protection was used when handling the Coumarin dye as its physical effects are not well understood.

### **Stagnation Flame Apparatus**

The stagnation plate was cleaned frequently of PIV alumina particles. It was found that the particles often coated the bottom of the plate, greatly increasing the level of scattered UV light entering the camera despite efforts to ensure the plate did not intersect the laser sheet. The nozzle and flow screens were cleaned periodically to reduce turbulence in the stagnation flame. Ideally, the entire flow delivery system should be cleaned of alumina particles prior to PLIF measurements to reduce the likelihood of Mie scattering off particles accidentally lofted into the flow.

Running the experiment for each fuel case required a significant amount of pressurized gas supply. Compressed air (extra dry 99.9% purity) and nitrogen (99%) were purchased from MEGS Specialty Gases Inc or Praxair. The NO/N<sub>2</sub> seeding

bottle (150 ppm NO,  $\pm 5\%$ ) was purchased from MEGS. All other specialty gases (25.8%, 30.0% and 42% O<sub>2</sub>/N<sub>2</sub> mixtures) were purchased from MEGS. Helium was used to pressurize the liquid fuel supply and was also purchased from MEGS. The alkane fuels (*n*-butane and *iso*-butane) were purchased from MEGS in smaller, low-pressure canisters. The liquid fuels (*n*-butanol and *iso*-butanol) were obtained from Sigma Aldrich.

## Appendix C: NO Seeding Settings

For calibration measurements, it is necessary to stabilize a lean calibration flame in the stagnation flame geometry while seeding a pre-defined concentration of NO into the flow. The calibration flame must contain premixed fuel and 21% O<sub>2</sub> to keep consistency with the other experiments. Therefore, the seeding concentrations were limited by the availability of enriched O<sub>2</sub>/N<sub>2</sub> gas cylinders.

There was one bottle of NO/N<sub>2</sub> gas at a concentration of 150 ppm of NO. There were three bottles of O<sub>2</sub>/N<sub>2</sub> - 25.8% O<sub>2</sub>, 30% O<sub>2</sub> and 42% O<sub>2</sub>. This allowed for three possible calibration concentrations. Table 6–1 contains the proportion required from supply gases and the NO seeding in the exit flow.

The absolute flow rates needed from each bottle is variable depending on the total flow rate required to stabilize the stagnation flame. In each seeding case, however, the proportion required from each bottle is the same. It should be noted that the amount of vaporized fuel in the final exit flow rate was assumed negligible.

Supplied Gases - Required Proportions (% total flow)				Exit Flow	
NO/N <sub>2</sub>	25.8% O <sub>2</sub> /N <sub>2</sub>	30.0% O <sub>2</sub> /N <sub>2</sub>	42.0% O <sub>2</sub> /N <sub>2</sub>	O <sub>2</sub> %	NO Conc. (ppm)
0.186047	0.813953			21	28
0.300000		0.700000		21	45
0.500000			0.500000	21	75

Table 6–1: NO Seeding Flows

## Appendix D: Manipulation of Chemical Kinetic Mechanisms

### Addition of Sub-mechanisms

Each mechanism used for Chemkin [18] contains several input files which are then combined in the software's pre-processor. When the NO<sub>x</sub> sub-mechanism (or any other sub-mechanism) is added to an existing mechanism, all of these files will need to be modified accordingly for successful pre-processing.

The \*.inp file contains a list of all chemical species and reactions. The reactions will have associated reaction rates, activation energies etc. – these can be modified as necessary. In the case of the NO<sub>x</sub> sub-mechanism addition, no modification to rates or energies were performed. The species of the NO<sub>x</sub> sub-mechanism were added to species list. The additional reactions associated with the NO<sub>x</sub> sub-mechanism were inserted into the existing \*.inp file behind the existing reactions.

The \*.dat files are compiled with the \*.inp file when the preprocessor is run. When the NO<sub>x</sub> species were added, corresponding data must be added to all \*.dat files as well. The two \*.dat files that were modified contained thermodynamic data and species transport data. The associated information was copied from the original sub-mechanism \*.dat files and added to the ones for the base mechanism. Note that the base mechanism values for transport and thermo data were used in the event of duplicate species and reactions during NO<sub>x</sub> sub-mechanism addition.

### Additional Notes

If the added reactions result in an error with the pre-processor, a \*.out file will be generated detailing the error. The mechanism files can then be modified to fix

the errors. If pre-processing is successful, the new mechanism is ready to be used in simulations.

If there are duplicated reactions, a decision must be made on which one to keep.

If there is duplicate thermodynamic or transport data, Chemkin [18] issues a warning and conveniently decides to accept the first instance while ignoring any other duplicates. Obviously, if this is not the desired outcome, the \*.dat files can be changed accordingly to eliminate the unwanted duplicates.

It was found that there can be a difference in the naming of species between the existing mechanism and the added sub-mechanism. For example, the Sarathy-Dagaut mechanism named a species SCH2 while the NO<sub>x</sub> sub-mechanism named it CH2(s) - these discrepancies need to be found and resolved. The final naming of the species is unimportant as long as the naming is consistent throughout all input files.

Cryptic write or compile errors in the pre-processor could be caused by line errors in any of the input files. It is possible that skipped lines or missing punctuation could lead to these types of errors. Good luck with these ones.

## Appendix E: Boundary Conditions for Simulation

Table 6–2 details the boundary conditions used for Chemkin [18] simulations of velocity and NO concentration profiles. These values were taken from experimental PIV data which had been post-processed with the DaVis software.

B.C. Input	<i>n</i> -butanol			<i>n</i> -butane		
	$\phi=0.8$	$\phi=1.0$	$\phi=1.3$	$\phi=0.8$	$\phi=1.0$	$\phi=1.3$
$T_{\text{flow}}$ (°C)	84	84	84	82	82	82
$T_{\text{plate}}$ (°C)	80	107	102	70	110	95
Axial Vel. (m/s)	0.6813	1.0634	1.0778	0.7389	0.9981	0.9672
Rad. Grad. Vel. (1/s)	39.8030	70.6530	74.0306	41.5190	61.5149	57.9177
D to Plate (mm)	13.3616	13.5915	13.3616	15.8700	15.6439	15.6439

Table 6–2: Boundary Conditions input into Chemkin simulations

## Appendix F: Quenching Corrections

The process for applying quenching corrections to the PLIF signal was developed when it was recognized that quenching is a significant factor which cannot be easily accounted for experimentally. Quenching corrections are necessary because the PLIF measurements do not account for the loss of quantum yield due to non-radiative collisions between two excited molecules. The measurement and derivation of quenching coefficients has been carried out in great detail in previously published works and will not be described herein. The process developed for this thesis involves the modelling of these coefficients through use of the LIFsim and Chemkin simulations.

Chemkin simulations are used to simulate several adiabatic flames of *n*-butanol and *n*-butane. The simulation provides knowledge of the peak temperature for each flame and the mole fraction of major quenching species ( $\text{O}_2$ ,  $\text{H}_2\text{O}$ ,  $\text{CO}$ ,  $\text{CO}_2$  and  $\text{N}_2$ ). Since mechanisms for *iso*-butanol were unavailable, it was assumed that the species and temperatures are the same between isomers. The Chemkin simulations were performed for both fuels at the three tested equivalence ratios, 0.8, 1.0 and 1.3.

These parameters were input in the LIFsim and the emission spectra was simulated for each case. The results were output and the peak relative LIF signal at the first band of fluorescence ( $\sim 236$  nm) was taken for processing. The peak LIF signals for stoichiometric and rich cases were divided by the lean LIF signal to determine the factor needed for quenching corrections. This correction factor,  $C_{corr}$  was applied its respective NO concentration measurements to result in the corrected NO

	<i>n</i> -butanol			<i>n</i> -butane		
Eq'm T(°K)	1924.197	2284.708	2160.546	1922.912	2294.519	2166.924
Mole Fraction N <sub>2</sub>	0.734	0.706	0.756	0.746	0.722	0.676
Mole Fraction O <sub>2</sub>	0.057	0.007	0.000	0.058	0.007	0.000
Mole Fraction H <sub>2</sub> O	0.113	0.151	0.159	0.106	0.142	0.147
Mole Fraction CO <sub>2</sub>	0.091	0.111	0.077	0.085	0.104	0.068
Mole Fraction CO	0.000	0.014	0.075	0.000	0.014	0.076
Max LIF signal	1.44E-16	1.12E-16	1.37E-16	1.52E-16	1.18E-16	1.36E-16
Corr. Factor $C_{corr}$	1.00	1.29	1.05	1.00	1.29	1.12

Table 6-3: Parameters generated by Chemkin simulations for quenching corrections and calculated correction factor

concentration profile. Please see Section 4.5 for the derivation of  $C_{corr}$ .

The use of this quenching correction does not correct for temperature twice. The calibration corrections correct for the change in LIF signal between room temperature and the temperature of the calibration (lean) flame. This quenching correction further corrects for the change in signal between the calibration flame temperature and that of a stoichiometric or rich flame.

## Appendix G: Recommendations

The most pressing issue that should be resolved is the non-uniformity in the laser sheet. The intensity distribution may be improved with the acquisition of beam conditioning equipment like a beam homogenizer. A technician from Newport may also be able to improve the beam distribution from the dye laser.

The collection optics can be improved in several ways. It is possible to achieve better magnification by purchasing a new UV collection lens. An achromatic lens can be purchased to further correct for chromatic aberrations in the fluorescence signal.

Better signal-to-noise ratio can be achieved by exciting with higher laser powers. The Nd:YAG pumping laser is currently used at approximately half the amplifier power – there is still plenty of power remaining there. The limiting factor in this case is the dye laser, where much of the power is lost generating the desired wavelength. Further research can be performed into finding an improved laser dye to use over Coumarin 450. Furthermore, during the writing of this thesis, it was found that the dye should be mixed with a methanol solvent if used at the desired wavelength of 452.00 nm. Switching to a methanol solvent could potentially increase the dye laser power.

Monitoring of laser power could be performed during the course of the experiment, reducing the uncertainty in laser power while measurements are being taken. Due to the scattered light off the detector in its current position, the detector head was replaced with a beam dump during measurements. The detector head measurements should also be checked again for accuracy and the optimum settings should

be found for powermeter readings.

Improvements to the PLIF procedure can also be performed to reduce uncertainty and increase signal-to-noise. During the excitation scan procedure in section 3.2.3, an operator subjectively determines the location of peak excitation. This method could be replaced with a better, more objective method of finding the excitation scan. Using the scan sequence in the dye laser, the signals obtained in the laser can be related to excitation wavelength by tracking the time required to scan between wavelengths. It is possible for a script to find images of maximum signal and relate that back to excitation wavelength.

To reduce the uncertainty in the calibration procedure, more calibration points can be used to determine the slope of the calibration curve. Data points can consist of additional seeded concentrations or can just be repeated measurements at the same concentration. In any case, given the variations in sheet intensity between days, it is probably still necessary to perform the calibration procedure before every day of experiment.

A better method of determining magnification of the collection optics is needed to accurately determine spatial position at every pixel. A suggested method would be using a fibre optic to direct UV light to excite a portion of seeded flow – the fibre optic, with its known diameter, can provide a more accurate magnification.

## References

- [1] B. E. Battles and R. K. Hanson. Laser-induced fluorescence measurements of NO and OH mole fraction in fuel-lean, high-pressure (1-10atm) methane flames - fluorescence modeling and experimental validation. *Journal of Quantitative Spectroscopy & Radiative Transfer*, 54(3):521–537, 1995.
- [2] L. J. Benezech, J. M. Bergthorson, and P. E. Dimotakis. Premixed laminar C<sub>3</sub>H<sub>8</sub>- and C<sub>3</sub>H<sub>6</sub>-air stagnation flames: Experiments and simulations with detailed kinetic models. *Proceedings of the Combustion Institute*, 32(1):1301–1309, 2009.
- [3] P. A. Berg, G. P. Smith, J. B. Jeffries, and D. R. Crosley. Nitric oxide formation and reburn in low-pressure methane flames. *Symposium (International) on Combustion*, 27(1):1377–1384, 1998.
- [4] J. M. Bergthorson and P. E. Dimotakis. Premixed laminar C<sub>1</sub>-C<sub>2</sub> stagnation flames: Experiments and simulations with detailed thermochemistry models. *Proceedings of the Combustion Institute*, 31(1):1139–1147, January 2007.
- [5] J. M. Bergthorson, D. G. Goodwin, and P. E. Dimotakis. Particle streak velocimetry and CH laser-induced fluorescence diagnostics in strained, premixed, methane-air flames. *Proceedings of the Combustion Institute*, 30(1):1637–1644, January 2005.
- [6] J. M. Bergthorson, S. D. Salusbury, and P. E. Dimotakis. Experiments and modelling of premixed laminar stagnation flame hydrodynamics. *Journal of Fluid Mechanics*, 681:340–369, 2011.
- [7] W. G. Bessler, C. Schulz, T. Lee, J. B. Jeffries, and R. K. Hanson. Strategies for laser-induced fluorescence detection of nitric oxide in high-pressure flames. I. A-X(0,0) excitation. *Applied Optics*, 41(18):3547–3557, 2002.
- [8] W. G. Bessler, C. Schulz, T. Lee, J. B. Jeffries, and R. K. Hanson. Strategies for laser-induced fluorescence detection of nitric oxide in high-pressure flames. II. A-X(0,1) excitation. *Applied Optics*, 42(12):2031–2042, 2003.

- [9] W. G. Bessler, C. Schulz, T. Lee, J. B. Jeffries, and R. K. Hanson. Strategies for laser-induced fluorescence detection of nitric oxide in high-pressure flames. III. comparison of A-X excitation schemes. *Applied Optics*, 42(24):4922–4936, 2003.
- [10] W. G. Bessler, V. Sick, and J. W. Daily. A versatile modeling tool for nitric oxide LIF spectra. *Proceedings of the Third Joint Meeting of the U.S. Sections of The Combustion Institute*, P105:1–6, 2003.
- [11] C. T. Bowman. Control of combustion-generated nitrogen oxide emissions: Technology driven by regulation. *Symposium (International) on Combustion*, 24(1):859–878, 1992.
- [12] M. J. Bradley and B. M. Jones. Reducing global NO<sub>x</sub> emissions: Developing advanced energy and transportation technologies. *AMBIO*, 31(2):141:149, 2002.
- [13] C. S. Cooper and N. M. Laurendeau. Laser-induced fluorescence measurements in lean direct-injection spray flames: technique development and application. *Measurement Science & Technology*, 11(7):902–911, 2000.
- [14] C. S. Cooper and N. M. Laurendeau. Parametric study of NO production via quantitative laser-induced fluorescence in high-pressure, swirl-stabilized spray flames. *Proceedings of the Combustion Institute*, 28:287–293, 2000.
- [15] C. S. Cooper, R. V. Ravikrishna, and N. M. Laurendeau. Comparisons of laser-saturated, laser-induced, and planar laser-induced fluorescence measurements of nitric oxide in a lean direct-injection spray flame. *Applied Optics*, 37(21):4823–4833, 1998.
- [16] F. H. V. Coppens, J. De Ruyck, and A. A. Konnov. The effects of composition on burning velocity and nitric oxide formation in laminar premixed flames of CH<sub>4</sub> + H<sub>2</sub> + O<sub>2</sub> + N<sub>2</sub>. *Combustion and Flame*, 149(4):409–417, June 2007.
- [17] P. Dagaut, S. M. Sarathy, and M. J. Thomson. A chemical kinetic study of *n*-butanol oxidation at elevated pressure in a jet stirred reactor. *Proceedings of the Combustion Institute*, 32(1):229–237, 2009.
- [18] Reaction Design. CHEMKIN-PRO, 2008.
- [19] M. D. DiRosa, K. G. Klavuhn, and R. K. Hanson. LIF spectroscopy of NO and O-2 in high-pressure flames. *Combustion Science and Technology*, 118(4-6):257–283, 1996.

- [20] A. El bakali, L. Pillier, P. Desgroux, B. Lefort, L. Gasnot, J. F. Pauwels, and I. da Costa. NO prediction in natural gas flames using GDF-kin3.0 mechanism NCN and HCN contribution to prompt-NO formation. *Fuel*, 85(7-8):896–909, 2006.
- [21] C. P. Fenimore. Formation of nitric oxide in premixed hydrocarbon flames. *Symposium (International) on Combustion*, 13(1):373–380, 1971.
- [22] B. Fishbein. Combustion of surrogate jet fuel components in premixed stagnation flames. Master’s thesis, McGill University, 2010.
- [23] D. Goodwin. Cantera: An object-oriented software toolkit for chemical kinetics, thermodynamics, and transport processes, 2009.
- [24] R. Grana, A. Frassoldati, T. Faravelli, U. Niemann, E. Ranzi, R. Seiser, R. Cattolica, and K. Seshadri. An experimental and kinetic modeling study of combustion of isomers of butanol. *Combustion and Flame*, 157(11):2137–2154, November 2010.
- [25] X. Gu, Z. Huang, S. Wu, and Q. Li. Laminar burning velocities and flame instabilities of butanol isomers-air mixtures. *Combustion and Flame*, 157(12):2318–2325, December 2010.
- [26] D. Healy, N. S. Donato, C. J. Aul, E. L. Petersen, C. M. Zinner, G. Bourque, and H. J. Curran. Isobutane ignition delay time measurements at high pressure and detailed chemical kinetic simulations. *Combustion and Flame*, 157(8):1540–1551, August 2010.
- [27] D. Healy, N. S. Donato, C. J. Aul, E. L. Petersen, C. M. Zinner, G. Bourque, and H. J. Curran. *n*-butane: Ignition delay measurements at high pressure and detailed chemical kinetic simulations. *Combustion and Flame*, 157(8):1526–1539, August 2010.
- [28] C. Ji, E. Dames, Y. L. Wang, H. Wang, and F. N. Egolfopoulos. Propagation and extinction of premixed C5-C12 *n*-alkane flames. *Combustion and Flame*, 157(2):277–287, February 2010.
- [29] Z. Klimont, J. Cofala, J. Xing, W. Wei, C. Zhang, S. Wang, J. Kejun, P. Bhandari, R. Mathur, P. Purohit, P. Rafaj, A. Chambers, M. Amann, and J. Hao. Projections of SO<sub>2</sub>, NO<sub>x</sub> and carbonaceous aerosols emissions in asia. *Tellus*, 61(4):602–617, 2009.

- [30] D. A. Knyazkov, A. G. Shmakov, I. V. Dyakov, O. P. Korobeinichev, J. De Ruyck, and A. A. Konnov. Formation and destruction of nitric oxide in methane flames doped with NO at atmospheric pressure. *Proceedings of the Combustion Institute*, 32(1):327–334, 2009.
- [31] A. A. Konnov. Implementation of the NCN pathway of prompt-NO formation in the detailed reaction mechanism. *Combustion and Flame*, 156(11):2093–2105, November 2009.
- [32] N. Lamoureux, A. El-Bakali, L. Gasnot, J. F. Pauwels, and P. Desgroux. Prompt-NO formation in methane/oxygen/nitrogen flames seeded with oxygenated volatile organic compounds: Methyl ethyl ketone or ethyl acetate. *Combustion and Flame*, 153(1-2):186–201, 2008.
- [33] Normand M Laurendeau. *Statistical Thermodynamics: Fundamentals and Applications*. Cambridge University Press, 2005.
- [34] S. A. Low and A. M. Isserman. Ethanol and the local economy. *Economic Development Quarterly*, 23(1):71–88, February 2009.
- [35] C. S. T. Marques, L. G. Barreta, M. E. Sbampato, and A. M. dos Santos. Laser-saturated fluorescence of nitric oxide and chemiluminescence measurements in premixed ethanol flames. *Experimental Thermal and Fluid Science*, 34(8):1142–1150, 2010.
- [36] C. S. T. Marques, L. R. dos Santos, M. E. Sbampato, L. G. Barreta, and A. M. dos Santos. Temperature measurements by OH LIF and chemiluminescence kinetic modeling for ethanol flames. *Quimica Nova*, 32:2073–2077, 2009.
- [37] C. S. McEnally and L. D. Pfefferle. Fuel decomposition and hydrocarbon growth processes for oxygenated hydrocarbons: butyl alcohols. *Proceedings of the Combustion Institute*, 30(1):1363–1370, January 2005.
- [38] J. A. Miller and C. T. Bowman. Mechanism and modeling of nitrogen chemistry in combustion. *Progress in Energy and Combustion Science*, 15(4):287–338, 1989.
- [39] L. V. Moskaleva and M. C. Lin. The spin-conserved reaction  $\text{CH} + \text{N}_2 = \text{H} + \text{NCN}$ : A major pathway to prompt no studied by quantum/statistical theory calculations and kinetic modeling of rate constant. *Proceedings of the Combustion Institute*, 28(2):2393–2401, 2000.

- [40] J. T. Moss, A. M. Berkowitz, M. A. Oehlschlaeger, J. Biet, V. Warth, P. Glaude, and F. Battin-Leclerc. An experimental and kinetic modeling study of the oxidation of the four isomers of butanol. *J. Phys. Chem. A*, 112(43):10843–10855, October 2008.
- [41] H. Mungekar and A. Atreya. NO formation in counterflow partially premixed flames. *Combustion and Flame*, 148(3):148–157, February 2007.
- [42] S. V. Naik and N. M. Laurendeau. Quantitative laser-saturated fluorescence measurements of nitric oxide in counter-flow diffusion flames under sooting oxy-fuel conditions. *Combustion and Flame*, 129(1-2):112–119, April 2002.
- [43] P. Osswald, H. Guldenberg, K. Kohse-Hoinghaus, B. Yang, T. Yuan, and F. Qi. Combustion of butanol isomers - a detailed molecular beam mass spectrometry investigation of their flame chemistry. *Combustion and Flame*, 158(1):2–15, January 2011.
- [44] S. H. Park, I. M. Youn, and C. S. Lee. Influence of ethanol blends on the combustion performance and exhaust emission characteristics of a four-cylinder diesel engine at various engine loads and injection timings. *Fuel*, 90(2):748–755, February 2011.
- [45] R. V. Ravikrishna, C. S. Cooper, and N. M. Laurendeau. Comparison of saturated and linear laser-induced fluorescence measurements of nitric oxide in counterflow diffusion flames. *Combustion and Flame*, 117(4):810–820, June 1999.
- [46] R. V. Ravikrishna, W. P. Partridge, and N. M. Laurendeau. Quantification of planar laser-induced fluorescence measurements of nitric oxide in laminar partially premixed flames. *Combustion Science and Technology*, 144(1-6):79–92, 1999.
- [47] R.V. Ravikrishna and N. M. Laurendeau. Laser-induced fluorescence measurements and modeling of nitric oxide in methane-air and ethane-air counterflow diffusion flames. *Combustion and Flame*, 120(3):372–382, February 2000.
- [48] J. R. Reisel, C. D. Carter, N. M. Laurendeau, and M. C. Drake. Laser-saturated fluorescence measurements of nitric-oxide in laminar, flat, C<sub>2</sub>H<sub>6</sub>/O<sub>2</sub>/N<sub>2</sub> flames at atmospheric-pressure. *Combustion Science and Technology*, 91(4-6):271–295, 1993.

- [49] J. R. Reisel and N. M. Laurendeau. Quantitative LIF measurements and modeling of nitric oxide in high-pressure C<sub>2</sub>H<sub>4</sub>/O<sub>2</sub>/N<sub>2</sub> flames. *Combustion and Flame*, 101(1-2):141–152, April 1995.
- [50] S. D. Salusbury. Premixed methane stagnation flames with oxygen enrichment. Master’s thesis, McGill University, 2010.
- [51] S. M. Sarathy, M. J. Thomson, C. Togbé, P. Dagaut, F. Halter, and C. Mounaim-Rousselle. An experimental and kinetic modeling study of *n*-butanol combustion. *Combustion and Flame*, 156(4):852–864, April 2009.
- [52] P. Saxena and F. A. Williams. Numerical and experimental studies of ethanol flames. *Proceedings of the Combustion Institute*, 31(1):1149–1156, January 2007.
- [53] C. Schulz, J. B. Jeffries, D. F. Davidson, J. D. Koch, J. Wolfrum, and R. K. Hanson. Impact of UV absorption by CO<sub>2</sub> and H<sub>2</sub>O on NO LIF in high-pressure combustion applications. *Proceedings of the Combustion Institute*, 29:2735–2742, 2002.
- [54] T. B. Settersten, B. D. Patterson, and W. H. Humphries. Radiative lifetimes of NO A<sub>2</sub>  $\sigma(v' = 0, 1, 2)$  and the electronic transition moment of the A<sub>2</sub> $\sigma$ -X<sub>2</sub> system. *Journal of Chemical Physics*, 131(10):104309–, September 2009.
- [55] R. Sivaramakrishnan, K. Brezinsky, G. Dayma, and P. Dagaut. High pressure effects on the mutual sensitization of the oxidation of NO and CH<sub>4</sub>-C<sub>2</sub>H<sub>6</sub> blends. *Phys. Chem. Chem. Phys.*, 9(31):4230–4244, 2007.
- [56] K. Skalska, J. S. Miller, and S. Ledakowicz. Trends in NO<sub>x</sub> abatement: A review. *Science of The Total Environment*, 408(19):3976–3989, September 2010.
- [57] D. D. Thomsen, F. F. Kuligowski, and N. M. Laurendeau. Background corrections for laser-induced-fluorescence measurements of nitric oxide in lean, high-pressure, premixed methane flames. *Applied Optics*, 36(15):3244–3252, May 1997.
- [58] D. D. Thomsen and N. M. Laurendeau. LIF measurements and modeling of nitric oxide concentration in atmospheric counterflow premixed flames. *Combustion and Flame*, 124(3):350–369, 2001.
- [59] S. R. Turns. Understanding NO<sub>x</sub> formation in nonpremixed flames: Experiments and modeling. *Progress in Energy and Combustion Science*, 21(5):361–385, 1995.

- [60] P. S. Veloo, Y. L. Wang, F. N. Egolfopoulos, and C. K. Westbrook. A comparative experimental and computational study of methanol, ethanol, and *n*-butanol flames. *Combustion and Flame*, 157(10):1989–2004, October 2010.
- [61] C. Vovelle, J. Delfau, and L. Pillier. Laminar hydrocarbon flame structure. *Combustion, Explosion, and Shock Waves*, 45:365–382, 2009. 10.1007/s10573-009-0047-z.
- [62] H. Wang, You X., A. V. Joshi, S. G. Davis, A. Laskin, F. Egolfopoulos, and C. K. Law. USC mech version II. high-temperature combustion reaction model of H<sub>2</sub>/CO/C<sub>1</sub>-C<sub>4</sub> compounds., May 2007.
- [63] Y. Yacoub, R. Bata, and M. Gautam. The performance and emission characteristics of C-1-C-5 alcohol-gasoline blends with matched oxygen content in a single-cylinder spark ignition engine. *Proceedings of the Institution of Mechanical Engineers Part A-journal of Power and Energy*, 212(A5):363–379, 1998.
- [64] B. Yang, P. Osswald, Y. Li, J. Wang, L. Wei, Z. Tian, F. Qi, and K. Kohse-Hoinghaus. Identification of combustion intermediates in isomeric fuel-rich premixed butanol-oxygen flames at low pressure. *Combustion and Flame*, 148(4):198–209, March 2007.
- [65] A. Yasar. Effects of alcohol-gasoline blends on exhaust and noise emissions in small scaled generators. *Metalurgija*, 49(4):335–338, October 2010.